Extreme multi-millennial slip rate variations on the Garlock fault, California: Strain super-cycles, potentially time-variable fault strength, and implications for system-level earthquake occurrence

James F. Dolan[1,*] (dolan@usc.edu), Lee J. McAuliffe[1,**], Edward J. Rhodes[2], Sally F. McGill[3], Robert Zinke[1]

1. Department of Earth Sciences, University of Southern California, Los Angeles, California, USA 90089
2. Department of Geography, University of Sheffield, Sheffield, S10 2TN, UK and Department of Earth, Planetary, and Space Sciences, UCLA, Los Angeles, California, USA 90095
3. Department of Geological Sciences, California State University San Bernardino, San Bernardino, California, USA 92407
*corresponding author
**now at: ConocoPhillipsAlaska, Anchorage, Alaska, USA 99501

Abstract

Pronounced variations in fault slip rate revealed by new measurements along the Garlock fault have basic implications for understanding how faults store and release strain energy in large earthquakes. Specifically, dating of a series of $26.0^{+3.5}/_{-2.5}$ m fault offsets with a newly developed infrared-stimulated luminescence method show that the fault was slipping at $>14.0^{+2.2}/_{-1.8}$ mm/yr, approximately twice as fast as the long-term average rate, during a previously documented cluster of four earthquakes 0.5-2.0 ka. This elevated late Holocene rate must be balanced by periods of slow or no slip such as that during the c. 3300-yr-long seismic lull preceding the cluster. Moreover, whereas a comparison of paleoseismic data and stress modeling results suggests that individual Garlock earthquakes may be triggered by periods of rapid San Andreas fault slip or very large-slip events, the "on-off" behavior of the Garlock suggests a longer-term mechanism that may involve changes in the rate of elastic strain accumulation on the fault over millennial time scales. This inference is consistent with most models of the geodetic velocity field, which yield slip-deficit rates that are much slower than the average latest Pleistocene-early Holocene (post-8–13 ka) Garlock slip rate of 6.5±1.5 mm/yr. These observations indicate the occurrence of millennia-long strain "super-cycles" on the Garlock fault that may be associated with temporal changes in elastic strain accumulation rate, which may in turn be controlled by variations in relative strength of the various faults in the Garlock-San Andreas-Eastern California Shear Zone fault system and/or changes in relative plate motion rates.

1. Introduction

The degree to which fault loading and strain release rates are constant in time and space is one the most fundamental, unresolved issues in modern tectonics. Analysis of faults reveals a wide range of behaviors, including: (1) relatively regular timing of earthquakes on some large strike-slip faults (e.g., Hartleb et al., 2003; 2006; Okumura et al., 2003; Scharer et al., 2010; 2011; Kozaci et al., 2011; Berryman et al., 2012; Rockwell, 2010); (2) clustering of large earthquakes on both single faults and regional fault networks (e. g., Marco et al., 1996; Rockwell et al., 2000; Dawson et al., 2003; Mason et al., 2004; Dolan et al., 2007; Tsutsumi & Sato, 2009; Ganev et al., 2010; Klinger et al., 2015); and (3) temporal variations in slip rate (e.g., Friedrich et al. 2003; Weldon et al., 2004; Mason et al., 2006; Gold and Cowgill, 2011; Onderdonk et al., 2015), illustrating the complexity of earthquake occurrence in time and space. Yet our current attempts to understand the mechanics of fault-system behavior remain severely data-limited. In particular, there are far too few data sets in which the timing of earthquakes can be compared directly with incremental fault slip rates. The pairing of these two types of data provides a complete dated path of deformation, yielding a record of the distribution of deformation through time – a key first step in understanding what controls these behaviors. In this paper we describe temporal variations in the slip rate of the Garlock fault, a major left-lateral fault that extends across the northern edge of the Mojave Desert in southern California. We compare these data with paleo-earthquake ages from a nearby trench site (Dawson et al., 2003) and discuss the implications of this paired data set for our understanding of the controls on earthquake occurrence in time and space.

2. The Garlock fault

The Garlock fault is one of the longest faults in southern California, extending eastward from its intersection with the San Andreas fault (SAF) for 250 km in a broad, northeast- to east-trending arc (Figure 1). Total documented sinistral displacement is 48-64 km (Smith, 1962; Smith and Ketner, 1970; Davis and Burchfiel, 1973; Carr et al., 1993; Monastero et al, 1997), with the onset of fault slip occurring sometime between 17 Ma and 10 Ma (Burbank and Whistler, 1987; Loomis and Burbank, 1988; Monastero et al., 1997; Frankel et al., 2008; Andrew et al., 2014). A prominent, ~2-km-wide extensional left step-over in the vicinity of Koehn Lake and a ~15º change in strike south of the Quail Mountains have been used to separate the Garlock fault into western, central, and eastern segments (McGill and Sieh, 1991) (Figure 1).

Although the Garlock fault exhibits abundant geomorphic evidence for recent activity (Clark, 1973; Clark and Lajoie, 1974; McGill and Sieh, 1991; McGill, 1992; Helms et al., 2003; McGill et al., 2009; Ganev et al., 2012; Madugo et al., 2012; Ritasse et al., 2014), it has not generated any significant earthquakes during the historic period. Several paleoseismologic studies, however, document evidence for large-magnitude earthquakes along the fault (McGill, 1992; McGill & Rockwell, 1998; Dawson et al., 2003; McGill et al., 2009; Madugo et al., 2012). The mid- to late Holocene earthquake history of the central part of the fault is particularly well recorded in a trench near El Paso Peaks (EPP), where Dawson et al. (2003), building on work initiated by McGill & Rockwell (1998), found evidence for six surface ruptures during the past 7,000 years. The four youngest surface ruptures comprise a cluster of events between ca. 500 and ~2,000 years ago. The most recent event (MRE) at their site occurred between AD 1450 and 1640, with the three earlier surface ruptures in the cluster occurring at AD 675-950, AD 250-475, and AD 25-275. The four-event cluster at the EPP trench was preceded by a 2,950–3,600-year-long lull, during which no surface ruptures occurred at the site. Two older surface ruptures occurred at 3340-2930 BC and 5300-4670 BC.

Several slip-rate studies along the Garlock fault yield similar preferred average slip rates since the latest-Pleistocene-early Holocene of ~5 to ~8 mm/yr for the central and western parts of the fault (Clark & Lajoie, 1974; McGill & Sieh, 1993; McGill et al., 2009; Ganev et al., 2012). At Clark Wash, along the eastern part of the western section of the Garlock fault ~30 km west of

Koehn Lake, McGill et al. (2009) reported a slip rate of $7.6^{+3.1}/_{-2.3}$ mm/yr based on radiocarbon dating of a 66±6 m offset of an incised channel. Farther east, Clark & Lajoie (1974) measured a latest Pleistocene lacustrine berm from pluvial Koehn Lake that has been offset by 80±5 m. Combining this offset with radiocarbon-dated tufa deposits and ostrocods yields a slip rate of ~5.0-7.7 mm/yr (after Ganev et al.'s [2012] application of dendrochronological calibration to the uncalibrated radiocarbon dates reported in Clark & Lajoie [1974]). At a site in the Summit Ranges 27 km east of Koehn Lake and 11 km east of the Dawson et al. (2003) El Paso Peaks trench site, Ganev et al. (2012) used the 58-70 m offset of a channel that is deeply incised into a latest Pleistocene alluvial fan with a 13.3 ka ^{10}Be depth-profile age to document a minimum slip rate of $5.3^{+1.0}/_{-2.5}$ mm/yr; consideration of potentially younger, climate-controlled incision events suggested a range of possible slip rates at their site from 5.1±0.3 mm/yr to 6.6±1.2 mm/yr. Still farther east along the central part of the fault, McGill and Sieh (1993) determined a slip rate of 4-9 mm/yr, with a preferred rate of 5-7 mm/yr, using a $90^{+16}/_{-8}$ 90+16/-8 m offset of a latest Pleistocene shoreline of Searles Lake and correlation of lake stands with radiocarbon-dated organic sediments from cores and shoreline features. It is noteworthy that all three of the slip rate sites located to the east of the westernmost site (McGill et al., 2009) yield rates that are slightly slower than McGill et al.'s (2009) rate. It is possible that this apparent geographic trend in rates is real, and reflects additional east-west extension north of the Garlock fault along the southernmost end of the Sierra Nevada frontal normal fault and similar faults to the east, consistent with the transform model for the Garlock fault of Davis & Burchfiel (1973). But the discrepancy lies within the error limits of all of these rates, and may not reflect a real westward increase in fault slip rate. All of these latest Pleistocene-early Holocene average slip rates, which collectively yield a range of possible rates from ~5 to ~8 mm/yr (hereafter expressed as ~6.5±1.5 mm/yr), are generally similar to much longer-term rates averaged over million-year time scales (Carter, 1994; Burbank & Whistler, 1987; Loomis & Burbank, 1988; Monastero et al.; 1997; Keenan; 2000). Recently, Ritasse et al. (2014) used soil ages and a single quartz OSL sample on a 30–37 m offset of a fluvial terrace at a site in the Slate Range 6 km east of the McGill and Sieh (1993) site to suggest a faster late Holocene (c. 3.5 ka) slip rate of 7-14 mm/yr, with a preferred rate of 11-13 mm/yr, hinting at potentially complex patterns of strain release along the central Garlock fault.

Such intermediate- and long-term geologic slip rates are inconsistent with most interpretations of geodetic data. Specifically, most analyses of the geodetic data have suggested little or no left lateral strain accumulation across the Garlock fault over the past several decades (Savage et al., 1981; 1990; 2001; Gan et al., 2000; Miller et al., 2001; Peltzer et al., 2001; McClusky et al., 2001; Meade and Hager, 2005; Loveless and Meade, 2011; but see Chuang and Johnson, 2011, Johnson, 2013, and Platt and Becker, 2013, for alternative assessments). Instead, the short-term geodetic data demonstrate that the region surrounding the Garlock fault is presently dominated by north-northwest-oriented right-lateral shear parallel to the eastern California shear zone, extending across the Garlock at a high angle (e.g., McGill et al., 2009).

3. Results

3.1 Christmas Canyon West Study Site – The Christmas Canyon West (CCW) study site is located along the central part of the Garlock fault 30 km southeast of Ridgecrest, California, and 2 km due west of Christmas Canyon at N35.52˚, W117.38˚ (Figures 1 & 2). We chose this site for several reasons. The site lies along a highly linear section of the fault where offsets of late Holocene alluvial fans and associated drainages are particularly well expressed (Figure 2; Clark, 1973; McGill and Sieh, 1991). This study focuses on two of these late Holocene alluvial fans and associated north-flowing drainages that have all been offset by left-lateral slip on the Garlock fault, which exhibits a prominent, linear main trace across the site (Figure 2). Minor secondary faulting ~250 m to the north does not exhibit any discernible left-lateral offset and appears only to accommodate normal slip, as expressed in several, low-relief, fault-parallel grabens. All of these features are readily discernible on high-resolution lidar digital topographic data collected along the Garlock fault as part of the U. S. National Science Foundation's GeoEarthScope project (data available at http://www.opentopography.org/). The use of these data greatly simplified our mapping of locally subtle topographic features.

Numerous well-defined offset gullies and intervening alluvial fan remnants are particularly well-expressed in the lidar imagery across the two fans at the CCW site (Figures 3 and 4). The remnant alluvial fan surfaces are generally quite planar, typically with less than ~10-15 cm of local topographic relief, most of which is related to subdued pebble-cobble bars relict from the original depositional bar-and-swale fan surface topography. A striking feature of the offset is that many 50- to 100-cm-deep gullies incised into the relict alluvial fan surfaces can be restored with a similar offset of $26.0^{+3.5}/_{-2.5}$ m (Figures 3–5; S2–S4). This overall offset is based on a combination of field work and 3D restorations of individual geomorphic features observable in the lidar data using the LaDiCaoz reconstoration tool (Zielke et al., 2015) . Specifically, the prominent alluvial fan remnant at Site 1 (location in figure 2), where we excavated sample pits 11A and 12C, as well as several other minor drainages and intervening alluvial bars (Figure 3A), are well restored with a visually preferred back-slip of $26.0^{+3.5}/_{-2.5}$ m (Figure 5A–B). The best-fitting back-slip value based on cross-correlation of topographic profiles in LaDiCaoz ($25.5^{+4.0}/_{-2.0}$ m) is similar to our visually preferred restoration (Figure 5C). The well-defined eastern edge of the offset alluvial fan and associated NE-flowing drainage at Site 1 are also well-restored by back-slip of $26.0^{+3.5}/_{-2.5}$ m (Figure 5D–E). In this case, the best-fitting back-slip value based on LaDiCaoz correlation ($26.0^{+3.5}/_{-2.5}$ m; Fig. 5F) agrees exactly with our visually preferred restoration at this site. On the eastern, Site 2 fan, back-slip of $26.0^{+3.5}/_{-2.5}$ m restores the prominent alluvial fan remnant on which we excavated pits 12A and 12B (Figures 4A and 5G–H), as well as a major NNE-flowing drainage on the eastern part of the fan and numerous smaller drainages incised into the fan surface. Our LaDiCaoz restoration of the alluvial fan remnant results in a similar optimal restoration of $25.7^{+3.8}/_{-2.2}$ m (Figure 5I). The error limits for each of our measurements were determined by restoring the offset feature far enough about the preferred value so as to yield sedimentologically and/or structurally unreasonable reconstructions; these values define the maximum and minimum-possible offsets and thus our error limits. The similarity in the offset of all of these features from two different alluvial fans confirms that these fans have experienced the same displacements since their deposition. We combine these two sets of displacements into our preferred offset across the CCW site of $26.0^{+3.5}/_{-2.5}$ m.

3.2. Age Control – At the Christmas Canyon West site, we excavated four $1 m^3$ pits into the two offset alluvial fans (Figures 3A & 4A). We were particularly careful to excavate the pits into the most planar parts of the relict alluvial fan surfaces farthest removed from the adjacent incised drainages. The sediments exposed within these pits in all cases consist of beige to pale brown, weakly stratified sand and sandy gravel. Bedding was defined by color and textural variations as well as by local horizontal to gently dipping pebble layers. From these pits we collected 17 luminescence dating samples, in each case as a vertical sequence of four samples (five for pit 11A) at different depths down to ~80 cm. Samples were collected in steel tubes tapped into the more sand-rich horizons, and in-situ gamma spectrometer measurements were conducted at each sample position to determine the dose rate. All samples were prepared and processed at the UCLA luminescence laboratory, and were dated with the post-IR_{50}-$IRSL_{225}$ single-grain luminescence dating method (Rhodes, 2015). This newly developed method facilitates accurate dating of feldspar grains with a precision equal in many cases to radiocarbon analysis of detrital charcoal, allowing us to date previously undatable strata and landforms (see Rhodes [2015] and Supplementary data for description of the post-IR_{50}-$IRSL_{225}$ technique).

At all of our sample sites, the IR_{50}-$IRSL_{225}$ luminescence ages reveal a layered fan structure composed of multiple alluvial deposits of mid- to late Holocene age. Age estimates show a high degree of internal consistency, providing confidence in these results (Table 1). Specifically, most sites had a ca. 3800 to 5,000-year-old deposit at ~0.4–0.85 m depth overlain by a much younger ca. 1900–2600-year-old deposit (Table 1; Figure 6). Several much younger ages [30 to 790 calendar years before AD 2013 [hereafter, yb2013]] from the shallowest 15 cm of pits 11A and 12C were collected from horizons that were paler in color, finer grained, and more friable than underlying strata. These characteristics suggest that these very young deposits may represent partial infilling of swales from the original bar-and-swale topography of the fan, perhaps with additional aeolian input. After sampling, we recognized that the oldest of these young samples (790±70 yb2013) had been collected across a boundary between the very young unit and older, more cohesive and slightly darker brown underlying alluvium. This sample yielded two distinct groupings of ages, indicating that the young deposit in Pit 11A is 790±70 yb2013, and the older, uppermost alluvial fan deposit is 2010±230 yb2013 (Figure 6). The youngest deposits exposed in the pits are clearly distinct from the underlying fluvial/alluvial strata, and we do not discuss these young ages further.

As noted above, the fan surfaces have clearly been incised after deposition and stabilization by 50 to 100-cm-deep, north-flowing streams. A trench excavated through pit 12A at site 2 and extending fault-parallel to the incised, active drainage to the east to illustrate this relationship revealed the sub-horizontal and laterally continuous deposits that demonstrate that the incision of these drainages, which define the offset features we measured, occurred after the deposition of the youngest alluvial deposit (Figure 7).

The youngest dates from the offset alluvial deposits come from Pit 12B. In that pit, an 1860±150 yb2013 sample comes from gently southeast-dipping strata that may represent the lateral propagation of an alluvial bar during alluvial fan deposition. A sample from slightly deeper, flat-lying alluvium in the same pit yielded a near-identical age of 1910±150 yb2013. Inasmuch as these samples were collected from alluvium that lies below the well-preserved relict fan surface, well removed from any recent incised drainages, they must pre-date the incision event.

3.3. Calculation of Slip Rates – The consistent $26.0^{+3.5}/_{-2.5}$ m left-lateral offset of numerous geomorphic features at CCW indicates that large portions of the landscape at the site have been displaced the same amount, and therefore have experienced the same number of surface ruptures. Thus, the youngest date from the youngest alluvial deposit forming the uppermost part of the offset fans (1860 ± 150 yb2013 in pit 12B [Table 1]) can be used as the limiting maximum age for the incision event that led to abandonment of deposition on these fans, and the resulting $14.0^{+2.2}/_{-1.8}$ mm/yr (uncertainty calculated in quadrature) slip rate represents the minimum rate for this stretch of the Garlock fault over this time interval. We note that use of either the slightly older sample from deeper in Pit 12B (1910±150 yb2013) or the youngest Unit 2 alluvial/fluvial sample from Pit 11A (2010±230 yb2013) as limiting constraints results in very similar minimum slip rate estimates ($13.6^{+2.1}/_{-1.7}$ mm/yr and $12.9^{+2.3}/_{-1.9}$ mm/yr, respectively). Moreover, the fact that the slightly older fan remnants documented in pits 12B (2280±140 yb2013), and 12A (2620±190 yb2013), have also been offset ~26 m indicates that there was no additional fault offset (and therefore no surface ruptures) during the 150- to 700-year-long period preceding deposition and abandonment of the youngest offset fan remnant we dated in Pit 12B at ca. 1900 yb2013.

4. Discussion and Conclusions

4.1. Temporally Variable Incremental Fault Slip Rates – The $14.0^{+2.2}/_{-1.8}$ mm/yr minimum late Holocene rate is about twice as fast as the preferred longer-term (averaged over past 8 to 13 ka) ~6.5±1.5 mm/yr rate of the central Garlock fault revealed by previous studies (Clark and Lajoie 1974; Clark et al., 1984; McGill and Sieh, 1993; McGill et al., 2009; Ganev et al., 2012). This comparison indicates that the fault was slipping much faster than its average rate during the same time interval as the occurrence of the ca. 500- to 2,000-year-old, four-event earthquake cluster observed at the Dawson et al. (2003) El Paso Peaks trench site. Although we cannot be certain that the rupture histories at EPP and CCW are identical, the 27 km distance between these sites is along a straight section of the fault with no structural complexities that would impede rupture or suggest segmentation of the fault. Moreover, the EPP site is 15 km east of the eastern end of the stepover between the western and central segments of the Garlock fault, so it seems unlikely that the EPP site would record ruptures from the western segment that failed to propagate all the way to CCW. Thus, it seems most likely that the post-1.9 ka period of rapid slip we document at CCW records slip during the four-event cluster observed at EPP. In addition, if the slip rate at the EPP site 27 km to the west is similar to what we document at CCW, as seems likely given the structural simplicity of the intervening stretch of the Garlock fault, then we can use small geomorphic offsets near the EPP site to further refine the incremental rate record (Figure 8). Specifically, near EPP McGill and Sieh (1991) measured groupings of offsets at 7 m, 14 m, and 18 m, which have been interpreted to record displacements in the three most-recent earthquakes of 7 m, 7 m, and 4 m, respectively (McGill and Sieh, 1991; Dawson et al., 2003; Ganev et al., 2012); we attribute the additional ~8 m of displacement at CCW (26 – 18 m) to the fourth event back, likely with some combination of somewhat different displacements in individual earthquakes at the two sites. Regardless of whether the exact same displacements occurred in these four earthquakes at the CCW and EPP sites, the IRSL ages indicate that the ~26 m of slip measured at CCW occurred during the same time period as the four-earthquake cluster observed at the Dawson et al. (2003) trench site.

We infer that the incision of the ca. 1900 yb2013 fan surfaces that are now offset $26.0^{+3.5}/_{-2.5}$ m at CCW likely occurred just prior to the fourth earthquake back (1740-1990 years ago; Dawson et al., 2003). This inference is justified because: (1) if the incision occurred after the fourth earthquake back, then the $26.0^{+3.5}/_{-2.5}$ m of slip would have occurred in only three earthquakes, which would require >8.5 m of slip per event, which is larger than that estimated by McGill &

Sieh (1991) for any part of the central Garlock fault; and (2) the fifth earthquake back at EPP occurred over 5000 years ago (Dawson et al., 2003), well before deposition of the incised features that are now offset ~26 m.

These observations indicate that the time period from the incision event at CCW to the present spans three complete earthquake cycles, plus a fourth open interval that will be completed when the next earthquake occurs. If we calculate the slip rate just using the closed, 1175-1615-year-long, three-event time window for the most recent three earthquakes in the cluster observed at the EPP site from Dawson et al. (2003) and the 18 m of slip suggested by analysis of small geomorphic offsets near the EPP trench (McGill & Sieh, 1991), then the resulting slip rate would be ~13.3 ± 1.6 mm/yr, similar to the $\geq 14.0^{+2.2}/_{-1.8}$ mm/yr rate described above.

Interestingly, in two of the only other sites where similar comparisons can be made between incremental fault slip rates and detailed paleo-earthquake ages along strike-slip faults, both the Awatere fault at Saxton River in New Zealand (Mason et al., 2004; 2006; Gold and Cowgill, 2011; Zinke et al., 2015) and the Mojave section of the San Andreas fault at Wrightwood (Weldon et al., 2004) exhibit similar behavior, with large variations in slip rate that span multiple earthquake cycles. Although the Awatere fault slip-rate data are based partially on potentially unreliable greywacke clast weathering-rind ages and the Wrightwood incremental rate data are derived from a region of complex, distributed faulting, the presence of similar, large (factor of 2-10X) variations in rate raises the possibility that this is a common behavior on strike-slip faults, perhaps masked until now by the paucity of such combined earthquake age-plus-incremental slip rate data sets. If true, such behavior has fundamental implications for our understanding of how faults store and release strain energy, as well as for the stress evolution of regional fault systems and the basic controls on the system-level occurrence of earthquakes in time and space, as discussed below. It is noteworthy that the fault displacements accommodated at these two sites during the periods of anomalously rapid slip (~20 m at Wrightwood and ~40 m at Saxton River) were grossly similar to the ~26 m of slip that occurred during the 0.5-2.0 ka cluster on the central Garlock fault, perhaps suggesting that this displacement range may represent an upper limit to whatever mechanism(s) control this behavior.

4.2. Earthquake supercycles and the relationship between variable fault slip rates and elastic strain accumulation rates – The combination of the CCW late Holocene rate data, the EPP paleo-earthquake ages, and previously published measurements of small geomorphic displacements and fault slip rates averaged over longer time periods allow us to construct detailed time-displacement histories for the central Garlock fault spanning mid- to late Holocene time (Figure 5). The resulting strain-release record shows that the Garlock fault experiences strain supercycles comprising multiple earthquakes and large fault displacements separated by millennia-long lulls.

But how do these highly variable fault slip rates relate to the rate of elastic strain accumulation along the Garlock fault? A common simplifying assumption in studies of earthquake recurrence patterns is that the rate of elastic strain accumulation remains relatively constant from earthquake cycle to earthquake cycle (e.g., Weldon et al., 2004; Goldfinger et al., 2013; Field et al., 2015). But is this basic assumption warranted? In the case of the Garlock fault, at least, perhaps not. As noted above, most geodetically constrained models of elastic strain accumulation have suggested to many researchers that the central Garlock fault is storing elastic strain energy at less than half of the latest Pleistocene-Holocene slip rate of ~6.5 ± 1.5 mm/yr (e.g., McClusky et al., 2001; Miller et al., 2001; Peltzer et al., 2001; Meade & Hager, 2005; Dolan et al., 2007; Oskin et al., 2008; McGill et al., 2009; Loveless and Meade, 2011). Moreover, the current geodetic velocity field shows primarily fault-perpendicular, northwest-southeast right-lateral shear (e.g., Savage et al., 1990; Peltzer et al., 2001; McGill et al., 2009), rather than obvious east-west, left-lateral elastic strain accumulation, as would be expected along the sinistral Garlock fault if it had a ductile root that was actively creeping today.

Some researchers (e.g., Chuang and Johnson [2011], Johnson [2013], and Platt & Becker [2013]) have suggested that this apparent transiently slow slip-deficit rate is not real, but the Platt and Becker (2013) model results do not match latest Pleistocene-Holocene geologic rates (Hatem and Dolan, 2015). The Johnson (2013) model gives slip rates for the Garlock fault that are comparable to Holocene rates for some segments if viscoelastic seismic cycle effects (e.g. Savage and Prescott, 1978) are taken into account. This is in large part because Johnson [2013] assumes that the Garlock fault is in the late stages of an earthquake cycle, as do Chuang and Johnson (2011). Considering the 3300-year-long, post-5 ka absence of earthquakes documented at EPP relative to current, ca. 450-year-long period since most recent earthquake at EPP, this may or may not be true. Also, it is worth noting that another study making use of different viscosity structures and earthquake chronologies suggests that viscoelastic earthquake cycle-related perturbations to surface velocities are too small to affect block model-inferred slip rates on the Garlock fault (Hearn et al., 2013).

If the apparent geologic-geodetic rate discrepancy for the Garlock fault is real, as suggested by most studies, the rate of elastic strain accumulation must vary significantly over the timescales of one to a few earthquakes, since the rates of strain accumulation and release must balance when averaged over numerous earthquakes. This discrepancy suggests that the Garlock fault may experience two different modes of behavior, with alternating periods of slower-than-average strain accumulation balanced by periods of faster-than-average rates.

4.3. Possible controls on earthquake supercycle behavior – These observations suggest the possibility that the rate of elastic strain accumulation in the seismogenic upper crust may be slower during lulls in earthquake activity and faster during clusters (e.g., Dolan et al. 2007). For example, if the c. 3,300-year-long lull in earthquake activity between c. 2 ka and 5 ka (Dawson et al., 2003) was characterized by an elastic strain accumulation rate that is much slower than the long-term average (similar to the current phase of slow strain accumulation), then strain accumulation rates must have been much faster than average during and/or immediately preceding the four-earthquake cluster observed at the El Paso Peaks site. Interestingly, geodetically constrained models of elastic strain accumulation along the Mojave section of the San Andreas fault suggest similar temporal variations in rate, with current rates being much slower than the long-term fault slip rate (e.g., Argus et al., 2005; Loveless and Meade, 2011). For example, Loveless and Meade (2011), using the Southern California Earthquake Center's comprehensive CFM-R model of 3D fault geometries, estimated a slip-deficit rate (referred to by some as a "geodetic slip rate") along the Mojave section of the SAF of only 16 mm/yr, relative to geologic slip rates on the Mojave section of ~30–40 mm/yr (Weldon et al., 2004; Weldon and Fumal, 2005; Sickler et al., 2006; Pruitt et al., 2009). Thus, as with the large variations in fault slip rate observed on both the Garlock and San Andreas faults (Weldon et al., 2004; this study), the rate of elastic strain accumulation may also vary significantly, beyond the level that might be expected from visco-elastic earthquake-cycle effects (e.g., Meade and Hager, 2004). These data fit the model of Dolan et al. (2007), in which they suggested that the Garlock and San Andreas act as a mechanically complementary, integrated pair, and that both faults are currently in periods of relatively slow strain accumulation and release.

Various mechanisms have been suggested to explain such behavior, focusing mainly on: (1) ways to alternately strengthen and weaken the fault either in the brittle, upper crust, or the ductile lower crust, or both; or (2) variations in the stress evolution of the system; or, more speculatively, (3) variations in the overall rate of energy input into the system (i.e., changes in relative plate motion rates). One example of the first type of mechanism, suggested by Dolan et al. (2007), is that the ductile roots of the fault strain harden during periods of rapid slip along the seismogenic parts of the fault (e.g., during an earthquake cluster), with strain hardening processes occurring at rates that temporarily overwhelm counteracting annealing processes. This leads to a lull in lower crustal ductile shear, and consequently in upper crustal strain accumulation and earthquakes. During such a lull, plate boundary strain is accommodated preferentially on other faults, and the fault experiencing the lull gradually weakens as a result of annealing (Dolan et al., 2007). This behavior could result in the relative strength of regional fault networks switching such that deep, ductile strain is accommodated on the weakest fault in the system at any given time (Dolan et al., 2007). Another possibility is that this behavior may be driven by the (random) occurrence of the first event in a cluster, which may serve to somehow weaken the lower crustal shear zone below the fault. For example, Oskin et al. (2008) suggested that the first earthquake in a cluster may release fluids downward into the ductile roots of the fault zone, weakening it and allowing faster creep rates, which in turn would drive faster elastic strain accumulation in the upper crust and more frequent earthquakes. Both of these potential mechanisms are consistent with the ductile roots of major faults being mechanically stronger during lulls and weaker at the onset of and/or during a cluster.

Several studies have suggested that strain release during individual earthquakes may lag behind the rate of elastic strain accumulation during the preceding interseismic period, leading to a well of "extra" elastic strain energy that can be released in either very large-magnitude events and/or brief earthquake clusters, with the crust effectively acting as an elastic strain capacitor (e.g., Cisternos et al., 2005; Fay and Humphreys, 2006; Sieh et al., 2008, Goldfinger et al., 2013). Indeed, it is difficult to explain observations such as the exceptionally fast SAF slip rate (~89 mm/yr) during the AD 600-900, five-earthquake pulse documented at Wrightwood by Weldon et al. (2004) without there being significant stored elastic strain energy available prior to the first earthquake in the sequence. However, while in our view the crust likely is capable of storing significant amounts of elastic strain energy, this mechanism, by itself, does not readily explain why faults would accumulate tens of meters of potential fault slip (i.e., elastic strain energy) prior to breaking in the first event of an anomalously rapid, multi-earthquake strain pulse. Unless there is some as-yet-unidentified mechanism by which upper crustal faults can strengthen over multiple earthquake cycles such that the fault becomes more resistant to slip during lulls (e.g., centennial- to millennial-term changes in constitutive properties of fault-zone rocks), and less resistant to slip during periods of rapid slip, this suggests that the rate of elastic strain accumulation may also increase just prior to and/or during the period of anomalously rapid slip.

Models of simulated patterns of seismicity suggest another possibility in which episodic, fundamental reorganizations of the mode of strain energy release are driven by changes in the entropy of stress distributions along the fault; small total variations in stress state along the fault (i.e., a relatively coherent stress field) will favor the occurrence of large-magnitude events involving long sections of the fault, whereas large variations in the state of stress (i.e., a highly irregular, disordered stress field) will favor periods of much lower strain release and a more random distribution of smaller earthquake magnitudes (Sornette & Sammis, 1995; Bowman et al., 1998; Dahmen et al., 1998; Ben-Zion et al., 1999; Sammis and Smith, 1999; Sammis & Sornette, 2002). Although this model is attractive for explaining the occurrence of any single large-magnitude earthquake (e.g., 2011 Mw 9.0 Tohoku, Japan), it fails to explain why the Garlock fault would generate four near-M_{max} ($\sim M_w \geq 7.5$) ruptures during a brief cluster.

Another possible model arises from the geologically complicated nature of plate boundary deformation in southern California. The storage and release of elastic strain energy on the Garlock fault in large earthquakes does not occur in isolation, and stress interactions from earthquakes on nearby faults will influence the behavior of the Garlock fault. At the latitude of the Garlock fault, relative plate boundary motion is dominated by slip on the San Andreas fault, which stores and releases energy 4-7 times faster than the Garlock fault (~30–40 mm/yr vs. ~5–8 mm/yr). Thus, any consistent changes in the Coulomb Failure Function (ΔCFF) "stressing rate" on the Garlock fault will be dominated by the effects of SAF slip.

For example, although the Weldon et al. (2004) slip-rate record for the Mojave section of the San Andreas fault at Wrightwood overlaps with only the most recent 1400 years of the central Garlock fault record, this allows comparison of at least the latter part of the 0.5-2 ka Garlock cluster. Interestingly, as shown in figure 9, the two most recent earthquakes in the Garlock cluster (dawson et al., 2003) correlate with a period of exceptionally rapid slip during a sequence of large SAF earthquakes (ca. 675-950 AD Garlock fault earthquake) and one of the largest-displacement earthquakes on the SAF in the Wrightwood record (ca. 1450-1640 AD Garlock fault earthquake). ΔCFF stress modeling (Rollins et al., 2011; McAuliffe et al., 2013) indicates that whereas slip on the SAF northwest of the Garlock fault intersection will inhibit slip on the Garlock fault, slip on the Mojave section of the SAF southwest of the Garlock intersection will encourage failure of the western part of the Garlock fault, and vice versa. Thus, periods of rapid slip on the Mojave section of the SAF may trigger individual earthquakes on the Garlock fault (or vice versa).

But what about longer-term stress interactions between the Garlock and San Andreas faults? At the multi-millennial time scales of the Garlock fault cluster and lull, displacement will occur in dozens of SAF "Big Ones" along the entire fault. Thus, the SAF can be viewed at these time scales as a continuously slipping feature. ΔCFF modeling of this situation demonstrates that slip along the entire central and southern SAF will encourage failure of the western Garlock fault (Lin & Stein, 2004), which in turn will encourage failure of the central Garlock fault (McAuliffe et al., 2013). Moreover, as noted above, the "Coulomb stressing rate" of the Garlock fault will be dominated by the behavior of the San Andreas fault, because of the much faster slip rate along the San Andreas.

Could the behavior of the Garlock fault be related to alternating periods of faster and slower slip on the San Andrea s, with attendant increases and decreases in ΔCFF stressing rate along the Garlock fault? In other words, could there be millennia-long periods of ΔCFF "stressing-rate enhancement" affecting the Garlock fault alternating with equally long-duration stressing-rate "shadows" caused by long-term decreases in SAF slip rate? If so, then clusters along the Garlock fault should correlate with periods of faster-than-average SAF slip rate, and Garlock fault lulls should occur when the SAF is slipping at a slower-than-average rate. Although the mid- to late Holocene SAF slip rate is not well constrained beyond a few key sites (e.g., Wallace Creek along the central SAF [Sieh & Jahns, 1984]; Little Rock Creek on the northwestern Mojave section of the SAF [Weldon & Fumal, 2005; Sickler et al., 2006; Pruitt et al., 2009]; Wrightwood along the southeastern part of the Mojave segment of the SAF [Weldon et al., 2004]), there is no evidence to suggest that the SAF was slipping faster than average during the 0.5-2 ka cluster or slower than average during the c. 2 – 5 ka Garlock fault lull. We emphasize, however, that more mid-Holocene incremental rate data are needed from the central and southern SAF to test this idea. Moreover, even if such data do come to light in future studies, this raises the question: Why would the SAF slow down significantly during the key period c. 2-5 ka, and then speed up during the 0.5-2.0 ka Garlock fault earthquake cluster? Such behavior might suggest that either the SAF was storing elastic strain energy more slowly than average during the Garlock fault lull, which in turn might suggest a stronger ductile root beneath the San Andreas fault during this period, or that the constitutive properties of the seismogenic part of the fault changed such that the SAF became more resistant to slip during the Garlock lull, thus reducing the Coulomb stressing rate on the Garlock fault caused by SAF slip.

Finally, although short-term relative plate motion rates documented by geodesy generally match those documented with much longer-term (million year) rates from global plate motion models (e.g., DeMets et al., 1994) along most plate boundaries (e.g., Sella et al., 2002), relative plate motion rates could potentially vary over the time scales we discuss here, perhaps in relation to clusters of extremely large earthquakes that temporarily modify the entire relative motion rate (e.g., Anderson, 1975). Comprehensive documentation of millennial fault slip rates along all faults in the plate boundary, similar to the compilation of Humphreys and Weldon (1994), together with geodynamical modeling that explicitly incorporates such behavior, may help address this possibility.

In summary, the major variations in incremental slip rate on the Garlock and San Andreas faults, together with evidence suggestive of potentially coordinated slip behavior and likely temporally transient strain accumulation along both faults, suggests that there may be multiple controls acting across a range of temporal and spatial scales. These include those processes modulating the timing and location of individual ruptures (e.g., Coulomb stressing-rate interactions), as well as longer-term controls that govern the timing and recurrence characteristics of earthquake clusters and the waxing and waning of elastic strain accrual and release rates. While the causes remain poorly understood, the increasing number of such observations suggests that such behaviors may be common, with basic implications for our understanding of how faults store and release strain energy. These results are particularly germane to probabilistic seismic hazard assessment, as we discuss below.

4.4. Implications for Probabilistic Seismic Hazard Assessment – Models of fault behavior based on the variability in earthquake recurrence intervals and displacements have long been used as the basis for renewal models used in probabilistic seismic hazard assessment (PSHA). Specifically, earthquakes have been suggested to be either time- or slip-predictable (Shimazaki & Nakata, 1980). That is, that the time to the next earthquake will depend on displacement in the previous event, or the slip in an earthquake depends on the time since the previous earthquake, respectively. While attractive in their simplicity, the reliability of these seismicity models remains a key unknown in current PSHA.

An important caveat to the applicability of these models is that they both assume a constant rate of elastic strain accumulation (i.e., a constant fault "loading" rate). Thus, if faults experience varying loading rates through time then these models cannot be used to accurately predict future events along that fault. As discussed above, both the Garlock and San Andreas faults may experience exactly such major variations in loading rates, rendering the use of time- and slip-predictable models problematic. Inasmuch as these are two of the best-documented faults in the world in terms of our ability to compare short-term geodetic and longer-term geologic rates, the violation of this underlying assumption in such models raises issues of basic concern regarding their continued use as primary inputs into PSHA.

Interestingly, as shown in figure 9, analysis of the Wrightwood incremental slip rate data from Weldon et al. (2004) suggests that within any 3- to 5-event strain cycle, whether faster or slower than average, the average rate within each interval is approximately matched at the time scale of individual earthquakes by slip in those earthquakes. In other words, the fault appears to be maintaining a relatively constant slip rate within each of these cycles. This observation would appear to be consistent with the notion of the fault "keeping up" with a relatively constant loading rate within any part of the strain cycle. In turn, this inference holds the promise of using such slip-deficit rates as key inputs into probabilistic seismic hazard assessments, with perhaps a better chance of forecasting the occurrence of future events relative to the use of long-term fault slip rates that average over multiple strain super-cycles. For example, it is noteworthy that the current extremely long open interval since the 1857 Fort Tejon earthquake (e.g., Scharer et al., 2010) is from the same section of the SAF from which geodetic slip-deficit rates indicate a much slower-than-average rate of elastic strain accumulation (e.g., Loveless and Meade, 2011). Such observations raise basic questions about the current state of probabilistic seismic hazard assessment strategies and suggest that future efforts consider the possibility of temporally variable loading rates.

If rates of elastic strain accumulation increase before or during clusters, and decrease during lulls, as appears likely based on the available data from the Garlock fault and the Mojave section of the San Andreas, then the recognition of such transiently variable fault loading rates becomes of paramount importance for developing more accurate seismic hazard forecasts. The need to recognize such strain transients, which we suspect may be quite subtle in some instances, highlights the importance of documenting detailed incremental geologic fault slip rates for use in comparison with shorter-term geodetic slip-deficit rates. Such comparisons hold the potential for determining as part of next-generation seismic hazard assessments whether a fault is acting in "slow" or "fast" mode, with commensurately lower or higher time-dependent seismic hazard.

Acknowledgements

This research was supported by the Southern California Earthquake Center. SCEC is funded by NSF Cooperative agreement EAR-0106924 and USGS Cooperative Agreement 02HQAG0008. The lidar data used in this study were collected by the National Center for Airborne Laser Mapping (NCALM) and are based on services provided by the Plate Boundary Observatory operated by UNAVCO for EarthScope and supported by the NSF (EAR-0350028 and EAR-0732947). We are grateful to Plamen Ganev, James Hollingsworth, Steven Okubo, and Evan Wolf for help in the field, to Wendy Barrera for assistance with luminescence sample preparation and analysis, to Charlie Sammis, Elizabeth Hearn, Alex Hatem, and Chris Rollins for helpful discussions, and to George Hilley and an anonymous reviewer for their thoughtful and constructive reviews. This SCEC contribution number XXXX.

References

Anderson, D.L., 1975 Accelerated plate tectonics: Science, v. 187, p. 1077-1079.

Andrew, J.E., Walker, J.D., Monastero, F.C., 2014, Evolution of the central Garlock fault zone, California: A major sinstral fault embedded in a dextral plate margin: Geol. Soc. Amer. Bull., v. 127(1-2), p. 227-249.

Argus, D.F., Heflin, M.B., Peltzer, G., Webb, F.H., and Crampe, F., 2005, Interseismic strain accumulation and anthropogenic motion in metropolitan Los Angeles: Jour. Geophys. Res., v. 101, doi: 10.1029/2003JB002934.

Berryman, K.R., Cochran, U.A., Clark, K.J., Biasi, G.P., Langridge, R.M., Villamor, P., 2012, Major earthquakes occur regularly on an isolated plate boundary fault: Science, v. 336: p. 1690-1693; doi: 10.1126/science.1218959.

Ben-Zion, Y., Dahmen, K., Lyakhovsky, V., Ertas, D., and Agnon, A., 1999, Self-Driven Mode Switching of Earthquake Activity on a Fault System: Earth Planet. Sci. Lett., v. 172/1-2, p. 11-21.

Bowman, D.D., G. Ouillon, C.G. Sammis, A. Sornette, and D. Sornette, 1998, An observational test of the critical earthquake concept: J.Geophys. Res., v. 103, p. 24,359-24,372.

Burbank, D.W., and Whistler, D.P., 1987, Temporally constrained rotations derived from magnetostratigraphic data: Implications for the initiation of the Garlock fault: Geology, v. 15, p. 1172–1175, doi: 10.1130/0091-7613.

Buylaert, J.P., Murray, A.S., Thomsen, K.J., & Jain, M., 2009, Testing the potential of an elevated temperature IRSL signal from K-feldspar: Radiation Measurements, v. 44, p. 560-565.

Carr, M.D., Harris, A.G., Poole, F.G., and R.J. Fleck, 1993, Stratigraphy and structure of Paleozoic outer continental margin rocks in Pilot Knob Valley, north central Mojave Desert, California: U.S. Geological Survey Bulletin, 2015, 33p.

Carter, B., 1994, Neogene offsets and displacement rates, central Garlock fault, California, in Geological investigations of an active margin, edited by McGill, S.F., and T.M. Ross, San Bernardino County Museum Association, Redlands, California, p. 348-356.

Chuang, R. Y., and Johnson, K. M., 2011, Reconciling geologic and geodetic model fault slip-rate discrepancies in Southern California: Consideration of nonsteady mantle flow and lower crustal fault creep: Geology, v. 39, p. 627-630.

Cisternos, M., Atwater, B.F., Torrejon, F., Sawai, Y., Machuca, G., Lagos, M., Eipert, A., Youlton, C., Salgado, I., Kamataki, T., Shishikura, M., Rajendan, C.P., Malik, J.K., Rizal, Y., and Husni, M., 2005, Predecessors of the giant 1960 Chile earthquake: Nature, v. 437, p. 404-407, doi: 10.1038/nature03943.

Clark, M.M., 1973, Map showing recently active breaks along the Garlock fault and associated faults, California, U.S. Geological Survey Miscellaneous Geological Investigations Map I-741, scale 1:24,000, 3 sheets.

Clark, M. M. and Lajoie, K. R. 1974, Holocene behavior of the Garlock fault: Geological Society of America, Abstracts with Programs, v. 6, p. 156-157.

Clark, M. M., et al., 1984, Preliminary slip-rate table and map of Late Quaternary faults of California: U. S. Geological Survey Open File Report, 84-106, 12 pp.

Dahmen, K., Erta, D., and Ben-Zion, Y., 1998, Gutenberg Richter and Characteristic Earthquake behavior in Simple Mean-Field Models of Heterogeneous Faults: Phys. Rev. E, v. 58, p. 1494-1501.

Davis, G.A., and Burchfiel, B.C., 1973, Garlock fault: An intracontinental transform structure, southern California: Geol. Soc. Amer. Bull., v. 84, p. 1407-1422, doi:10.1130/0016-7606.

Dawson, T.E., McGill S.F. & Rockwell, T.K., 2003, Irregular recurrence of paleoearthquakes along the central Garlock fault near El Paso Peaks, California: Jour. Geophys. Res., v. 108, p. 2356–2385.

DeMets, C., Gordon, R.G., Argus, D.F., and Stein, S., 1994, Effect of recent revisions to the geomagnetic reversal time scale on estimates of current plate motions: Geophys. Res. Lett., v. 21, p. 2191-2194.

Dolan, J.F., Bowman, D.D., and Sammis, C.G., 2007, Long-range and long-term fault interactions in Southern California: Geology, v. 35(9), p. 855-858.\

Fay, N., and Humphreys, E., 2006, Dynamics of the Salton block: Absolute fault strength and crust-mantle coupling in Southern California: Geology, v. 34, p. 261-264, doi: 10.1130/G22172.1.

Field, E.H., Biasi, G.P., Bird, P., Dawson, T.E., Felzer, K.R., Jackson, D.D., Johnson, K.M., Jordan, T.H., Madden, C., Michael, A.J., Milner, K.R., Page, M.T., Parsons, T., Powers, P.M. Shaw, B.E., Thatcher, W.R., Weldon R.J. II, and Zeng, Y., 2015, Long-term time-dependent probabilities for the third Uniform California Earthquake Rupture Forecast (UCERF3): Bull. Seismol. Soc. Amer., v. 105(2A), p. 511-543, doi: 10.1785/0120140093.

Frankel, K.L., Glazner, A.F., Kirby, E., Monastero, F.C., Strane, M.D., Oskin, M.E., Unruh, J.R., Walker, J.D., Anandakrishnan, S., Bartley, J.M., Coleman, D.S., Dolan, J.F., Finkel, R.C., Greene, D., Kylander-Clark, A., Morrero, S., Owen, L.A., and Phillips, F., 2008, Active tectonics of the eastern California shear zone, in Duebendorfer, E.M., and Smith, E.I., eds., Field Guide to Plutons, Volcanoes, Faults, Reefs, Dinosaurs, and Possible Glaciation in Selected Areas of Arizona, California, and Nevada: Geol. Soc. Amer. Field Guide 11, p. 43–81, doi: 10.1130/2008.fl d011(03).

Friedrich, A.M., Wernicke, B.P., and Niemi, N.A., 2003, Comparison of geodetic and geologic data from the Wasatch region, Utah, and implications for the spectral character of Earth deformation at periods of 10 to 10 million years: Jour. Geophys. Res,, v. 108(B4), p. 2199, doi:10.1029/ 2001JB000682.

Gan, W., Svarc, J.L., Savage, J.C., Prescott, W.H., 2000, Strain accumulation across the eastern California shear zone at latitude 36º30'N: Jour. Geophys. Res., v. 105, p. 16,229-16,236.

Ganev, P.N., Dolan, J.F., Blisniuk, K., Oskin, M., and Owen, L.A., 2010, Paleoseismologic evidence for multiple Holocene earthquakes on the Calico fault: Implications for earthquake clustering in the Eastern California shear zone: Lithosphere, v. 2, p. 287-298.

Ganev, P. N., J. F. Dolan, S. F. McGill, a nd K, L, Frankel, 2012, Constancy of geologic slip rate along the central Garlock fault: implications for strain accumulation and release in southern California: Geophys. Jour. Int., v. 190, p. 745-750.

Gold, R. D., and Cowgill, E., 2011, Deriving fault-slip histories to test for secular variation in slip, with examples from the Kunlun and Awatere faults: Earth and Planetary Science Letters, v. 301, p. 52-64.

Goldfinger, C., Ikeda, Y., Yeats, R.S., and Ren, J., 2013, Superquakes and Supercycles: Seismol. Res. Lett., v. 84, p. 24-32, doi: 10.1785/0220110135.

Hartleb, R.D., Dolan, J.F., Akyüz, S., and Yerli, B., 2003, A 2,000 year record of earthquake occurrence along the central North Anatolian fault, from trenches at Alayurt, Turkey: Bull. Seismol. Soc. Amer., v. 93, p. 1935-1954.

Hartleb, R.D., Dolan, J.F., Kozaci, O., Akyuz, S., and Seitz, G., 2006, A 2,500-year-long paleoseismologic record of large, infrequent earthquakes on the North Anatolian fault at Cukurcimen, Turkey: Geol. Soc. Amer. Bull., v. 118, p. 823-840.

Hatem, A.E. and Dolan, J.F., 2015, Garlock fault: What is your deal?: Southern California Earthquake Center 2015 Annual Meeting Proceedings, v. XXV, Poster 233 [Abstract].

Hearn, E. H., Pollitz, F. F., and Thatcher, W. R., 2013, How do "ghost transients" from past earthquakes affect GPS slip rate estimates on southern California faults?: Geochemistry, Geophysics, Geosystems, v. 14(4), p. 828-838. doi: 10.1002/ggge.20080.

Helms, J.G.,. McGill, S.F., and Rockwell, T.K., 2003, Calibrated, late Quaternary age indices using clast rubification and soil development on alluvial surfaces in Pilot Knob Valley, Mojave Desert, southeastern California: Quaternary Research, v. 60, no.3, p. 377-393.

Humphreys, E. D., and Weldon, R. J., 1994, Deformation across the western United States: A local estimate of Pacific-North America transform deformation: Jour. Geophys. Res., v. 99, p. 19,975-20,010.

Johnson, K.M., 2013, Slip rates and off-fault deformation in Southern California inferred from GPS data and models: Jour. Geophys. Res., v. 118(10), p. 5643-5664, doi: 10.1002/jgrb.50365.

Keenan, D.L., 2000, The geology and geochemistry of volcanic rocks in the Lave Mountains, California: Implications for Miocene development of the Garlock fault [M.S. Thesis], University of Nevada, Las Vegas, 81 p.

Klinger, Y., Le Beon, M., and Al-Qaryouti, 2015, 5000 yr of paleoseismicity along the Dead Sea fault: Geophys. Jour. Intnl., v. 202, p. 313-327, doi: 10.1093/gji/ggv134.

Kozaci, Ö., Dolan, J.F., Yönlü, Ö, and Hartleb, R. D., 2011, Paleoseismologic evidence for the relatively regular recurrence of infrequent, large-magnitude earthquakes on the eastern North Anatolian fault at Yaylabeli, Turkey: Lithosphere, doi: 10.1130/L118.1.

Lin, J., and Stein, R.S., 2004, Stress triggering in thrust and subduction earthquakes and stress interaction between the southern San Andreas and nearby thrust and strike-slip faults: Jour. Geophys. Res., v. 109, B02303, doi:10.1029/2003JB002607.

Loomis, D.P., and Burbank, D.W., 1988, The stratigraphic evolution of the El Paso basin, southern California: Implications for the Miocene development of the Garlock fault and uplift of the Sierra Nevada: Geol. Soc. Amer. Bull., v. 100, p. 12–28, doi: 10.1 130/0016-7606.

Loveless, J.P. and Meade, B.J., 2011, Stress modulation on the San Andreas fault by interseismic fault system interactions: Geology, 39(11), 1035–1038, doi:10.1130/G32215.1.

Madugo, C.M., Dolan, J.F., and Hartleb, R.D., 2012, New Paleoearthquake Ages from the Western Garlock Fault: Implications for Regional Earthquake Occurrence in Southern California: Bull. Seismol. Soc. Amer., v. 102, p. 2282-2299.

Marco, S., Mordechai, S., and Agnon, A., 1996, Long-term earthquake clustering: A 50,000-year paleoseismic record in the Dead Sea graben: Jour. Geophys. Res., v. 101, p. 6179-6191.

Mason, D.P.M., Little, T.A., and Van Dissen, R.J., 2004, Influence of a fault-segment junction on the rupturing behaviour of the Awatere fault, New Zealand, and displacement-length measurement for the Marlborough earthquake rupture of 1848: New Zealand Earthquake Commission Research Report No. 01/442, 148 p.

Mason, D.P.M., Little, T.A., and Van Dissen, R.J., 2006, Rates of active faulting during late Quaternary fluvial terrace formation at Saxton River, Awatere fault, New Zealand: Geol. Soc. Amer. Bull, v. 118, p. 1431-1446.

McAuliffe, L.J., Dolan, J.F., Kirby, E., Rollins, C., Haravitch, B., Alm, S. and Rittenour, T.M., 2013, Paleoseismology of the southern Panamint Valley fault: Imwplications for regional earthquake occurrence and seismic hazard in southern California: Jour. Geophys. Res., v. 118, doi:10.1002/jgrb.50359

McClusky, S.C., Bjornstad, S.C., Hager, B.H., King, R.W., Meade, B.J., Miller, M.M., Monastero, F.C. & Souter, B.J., 2001, Present day kinematics of the Eastern California Shear Zone from a geodetically constrained block model: Geophys. Res. Lett., v. 28, p. 3369–3372.

McGill, S.H.F., 1992, Paleoseismology and neotectonics of the central and eastern Garlock fault: Calif. Inst. of Technol., Pasadena, Calif., [Ph.D. dissertation], 235 pp., 1992.

McGill, S.F., and Sieh, K. E., 1991, Surficial offsets on the central and eastern Garlock fault near El Paso Peaks, California: Jour. Geophys. Res., v.103, p. 7265-7279.

McGill, S.F., and Sieh, K. E., 1993, Holocene slip rate of the central and eastern Garlock fault associated with prehistoric earthquakes. Jour. Geophys. Res., v. 96 (21), p. 597-21,621.

McGill, S.F., and Rockwell, T., 1998, Ages of late Holocene earthquakes on the central Garlock fault near El Paso Peaks, California, J. Geophys. Res., v. 103, B4, p. 7265-7279.

McGill, S. F., Wells, S. G., Fortner, S. K., Kuzma, H. A., and McGill J. D., 2009, Slip rate of the western Garlock fault, at Clark Wash, near Lone Tree Canyon, Mojave Desert, California. Geol. Soc. Amer. Bull., v. 121, p. 536-554.

Meade, B.J., and Hager, B.H., 2004, Viscoelastic deformation for a clustered earthquake cycle: Geophys. Res. Lett., v. 31, L10610, doi:10.1029/2004GL019643

Meade, B.J., and Hager, B.H., 2005, Block models of crustal motion in southern California constrained by GPS measurements: Jour. Geophys. Res., 110, B03403, doi:10.1029/2004JB003209.

Miller, M.M., Johnson, D.J., Dixon, T.H. & Dokka, R.K., 2001, Refined kinematics of the eastern California shear zone from GPS observations, 1993–1994: Jour. Geophys. Res., v. 106, p. 2245–2263.

Monastero, F.C., Sabin, A.E., and Walker, J.D., 1997, Evidence for post-early Miocene initiation of movement on the Garlock Fault from offset of the Cudahy Camp Formation, east-central California: Geology, v. 25, p. 247–250, doi: 10.1130/0091-7613.

Okumura, K., Rockwell, T.K., Duman, T.Y., Tokay, F., Kondo, H., & Yildirim, C., 2003, Refined Slip History of the North Anatolian Fault at Gerede on the 1944 rupture: EOS Transactions of the AGU, Fall 2003 meeting [abstract].

Onderdonk, N., McGill. S., and Rockwell, T., 2015, Short-term variations in slip rate and size of pre-historic earthquakes during the past 2000 years on the northern San Jacinto fault zone, a major plate boundary structure in southern California: Lithosphere, v. 7.3, p. 211-234, doi:10.1130/L393.1.

Oskin, M., Perg, L., Shelef, E., Strane, M., Gurney, E., Singer, B., and X. Zhang, X., 2008, Elevated shear zone loading rate during an earthquake cluster in eastern California: Geology, v. 36(6), p. 507-510.

Peltzer, G., Crampe, F., Hensley, S. & Rosen, P., 2001, Transient strain accumulation and fault interaction in the Eastern California shear zone: Geology, v. 29, p. 975–978.

Platt, J.P., and T.W. Becker, 2013, Kinematics of rotating panels of E-W faults in the San Andreas system: what can we tell from geodesy?: Geophys. Jour. Int., v. 194, p. 1295-1301.

Pruitt, A.H., Scharer, K.M., Fumal, T.E., Weldon, R.J., Gilleland, C.L., and Sickler, R., 2009, Microgeomorphic reconstruction to determine slip rate on the San Andreas fault near Littlerock, CA: 2009 SCEC Annual Meeting poster, 1-125.

Rhodes, E.J., 2015, Dating sediments using potassium feldspar single-grain IRSL: Initial methodological considerations: Quaternary International, v. 362, p. 14-22.

Rittasse, W.M., Kirby, E., McDolald, E., Walker, J.D., Gosse, J., Spencer, J.Q.G., and Herrs, A.J., 2014, Temporal variations in Holocene slip rate along the central Garlock fault, Pilot Knob Valley, California: Lithosphere, v. 6, p. 48-58

Rockwell, T.K., Lindvall, S., Herzberg, M., Murbach, D., Dawson, T., and Berger, G., 2000, Paleoseismology of the Johnson Valley, Kickapoo, and Homestead Valley Faults: Clustering of Earthquakes in the Eastern California Shear Zone: Bull. Seismol. Soc. Am. 90, 1200-1236.

Rockwell, T.K., 2010, The Non-Regularity of Earthquake Recurrence in California: Lessons From Long Paleoseismic Records in Simple vs. Complex Fault Regions: EOS Transactions of the AGU, Fall 2010 meeting [abstract].

Rollins, J.C., Ely, G.P., and Jordan, T.H., 2011, Coulomb stress interactions between simulated M>7 earthquakes and majors faults in Southern California: EOS Transactions of the AGU, Fall Meeting 2011, abstract #S21D-05.

Sammis, C.G., and Smith, S.W., 1999, Seismic Cycles and the Evolution of Stress Correlation in Cellular Automaton Models of Finite Fault Networks: Pure Appl. Geophys., v. 155, p. 307-334.

Sammis, C.G. and Sornette, D., 2002, Postitive feedback, memory, and the predictability of earthquakes: Proceedings of the National Academy of Sciences, v. 99, p. 2501-2508.

Savage, J. C., and W. H. Prescott, 1978, Asthenosphere readjustment and the earthquake cycle: Jour. Geophys. Res., v. 78, p. 3369– 3376.

Savage, J.C., Prescott, W.H., Lisowski, M. and King, N.E., 1981, Strain accumulation in southern California, 1973-1980: Jour. Geophys. Res., v. 86, p. 6991-7001.

Savage, J.C., Prescott, W.H. and Lisowski, M., 1990, An apparent shear zone trending north-northwest across the Mojave Desert into Owens Valley, eastern California: Geophys. Res. Lett., v.17, p. 2113-2116.

Savage, J.C., Gan, W., and Svarc, J.L., 2001, Strain accumulation and rotation in the Eastern California Shear Zone: Jour. Geophys. Res., v. 106, p. 21,995–22,007, doi: 10.1029/2000JB000127.

Scharer, K.M., Biasi, G.P., Weldon, R.J., Fumal, T.E., 2010, Quasi-periodic recurrence of large earthquakes on the southern San Andreas fault: Geology, v. 38, p. 555-558.

Scharer, K.M., Biasi, G.P., Weldon, R.J., 2011, A reevaluation of the Pallett Creek earthquake chronology based on new AMS radiocarbon dates, San Andreas fault, California: Jour. Geophys. Res., v. 116, B12111.
Shimazaki, K., and Nakata, T., 1980, Time-predictable recurrence model for large earthquakes: Geophys. Res. Lett., v. 7, p. 279–282.
Sickler, R., Weldon, R., Fumal, T., Schwartz, D., Mezger, L., Alexander, J., Biasi, G., Burgette, R., Goldman, M., Saldana, S., 2006, Slip rate of the San Andreas Fault near Littlerock, California: Seismol. Res. Lett., v. 77(2), p. 250-251.
Sella, G.F., Dixon, T.H., and Mao, A., 2002, REVEL: A model for recent plate velocities from space geodesy: Jour. Geophys. Res., v. 107, doi: 10.1029/2000JB000033.
Sieh, K.E., and Jahns, R.H., 1984, Holocene activity of the San Andreas fault at Wallace Creek, California: Geol. Soc. Amer. Bull., v. 95, p. 883-896.
Sieh, K., Natawidjaja, D.H., Meltzner, A.J., Shen, C.-C., Cheng, H., Li, K.-S., Suwargadi, B.W., Galetzka, J., Philibosian, B., Edwards, R.L., 2008, Earthquake supercycles inferred from sea-level changes recorded in the corals of West Sumatra: Science, v. 322, p. 1674-1678.
Smith, G.I., 1962, Large lateral displacement on Garlock fault, as measured from offset dyke swarm: Amer. Assoc. Petrl. Geol. Bull., v. 46, p. 85-104.
Smith, G.I., and Ketner, K.B., 1970, Lateral displacement on the Garlock fault, southeastern California, suggested by offset sections of similar metasedimentary rocks: U.S. Geol. Surv. Professional Paper 700-D, D1-D9.
Sornette, D., and Sammis, C.G., 1995, Complex critical exponents from renormalization group theory of earthquakes; implications for earthquake predictions: Jour. Phys. I France, v. 5, p. 607-619.
Tsutsumi, H., and Sato. T., 2009, Tectonic geomorphology of the southernmost Sagaing fault and surface rupture associated with the May 1930 Pegu (Bago) earthquake, Myanmar: Bull. Seismol. Soc. Amer., v. 99, ps. 2155-2168, doi: 10.1785/0120080113.
Weldon, R., Scharer, K., Fumal, T., and Biasi, G., 2004, Wrightwood and the earthquake cycle: What a long recurrence record tells us about how faults work: GSA Today, v. 14, doi: 10.1130/1052-5173.
Weldon, R., and Fumal, T., 2005, Slip rate of the San Andreas fault near Littlerock, California: Southern California Earthquake Center Proceedings and Abstracts, 2005 SCEC Annual Meeting, v. XV, p. 198.
Zielke, O., Y. Klinger, and J R. Arrowsmith, J.R., 2015, Fault Slip and Earthquake Recurrence Along Strike-Slip Faults --Contributions of High-Resolution Geomorphic Data: Tectonophysics, v. 638, p. 43-62, http://dx.doi.org/10.1016/j.tecto.2014.11.004.
Zinke, R., Dolan, J.F., Van Dissen, R., McGuire, C., Rhodes, E., Hatem, A., Grenader, J., and Langridge, R., 2015, Lidar and Luminescence Dating Analysis of Latest Pleistocene-Holocene Slip Rates on the Awatere fault at Saxton River, South Island, New Zealand; EOS Transactions, Proceedings of the Fall 2015 Annual Meeting, abstract T31A-2830.

Figure captions

Figure 1. Map of the Garlock fault (white) and other major active faults (gray) around the Mojave region of southern California, including the Mojave section of the San Andreas fault (SAF). White star shows location of Christmas Canyon West (CCW) study area. White circles shows locations of other slip-rate sites; CW is Clark Wash site of McGill et al. (2009); KL is

Koehn Lake site of Clark and Lajoie (1974); SR is Summit Range site of Ganev et al. (2012; their site 449100); SLS is Searles Lake shoreline site of McGill and Sieh (1993); and SLR is Slate Range site of Ritasse et el. (2013). White squares show locations of paleoseismic sites at El Paso Peaks (EPP) 27 km west of CCW site (Dawson et al., 2003) along the central Garlock fault, at Wrightwood (W) on Mojave section of SAF (Weldon et al., 2004), and at Twin Lakes (TL) along western Garlock fault (Madugo et al., 2012). B – Barstow; M – Mojave; R – Ridgecrest; T – Trona.

Figure 2. Interpreted GeoEarthScope lidar hillshade image of the Christmas Canyon West study area showing the two main study sites. Figure is centered on the main fault trace at N35.5213°, W117.383°. Colors show different alluvial fan surfaces mapped on the basis of lidar data, color aerial photographs, and field work. Faults mapped on lidar data shown by red lines. No obvious left-lateral displacement is observed on the secondary faults to the north of the main strand; these appear to accommodate only normal dip-slip. Boxes outline detailed study sites 1 and 2 discussed in text.

Figure 3. Interpreted GeoEarthScope lidar hillshade (A and B) and slope-aspect (C and D) maps of the western Site 1 at Christmas Canyon West study site (white star in Figure 1; detailed location of site shown in figure 2). Different colors on the slope aspect maps show the azimuth at which that point on the landscape is sloping. A and C show current topography; B and D show the landscape after restoration of preferred 26 m of fault slip at this site (see text for discussion). Colors in A and B denote interpreted alluvial fan surfaces (see also figure 2). White squares in A indicate locations of luminescence sample pits 11A and 12C.

Figure 4. Interpreted GeoEarthScope lidar hillshade (A and B) and slope-aspect (C and D) maps of eastern Site 2 at Christmas Canyon West study site (white star in Figure 1; detailed location of site shown in figure 2). Different colors on the slope aspect maps show the azimuth at which that point on the landscape is sloping. A and C show current topography; B and D show the landscape after restoration of preferred 26 m of fault slip at this site (see text for discussion). Colors in A and B denote interpreted alluvial fan surfaces (see also figure 2). White squares in A indicate locations of luminescence sample pits 12A and 12B; dashed box indicates location of small trench (figure 8) extending eastward from sample pit 12A excavated parallel to the fault to document relationship between incised, offset drainages and internal fan stratigraphy.

Figure 5. Restorations of geomorphically prominent offset features at CCW using the LaDiCaoz tool (Zielke et al., 2015). (A–C) Restoration of alluvial fan remnants and associated incised drainages at western CCW Site 1; (D–F) restoration of incised drainage defining southeastern edge of alluvial fan remnant at CCW Site 1, ~85 m east of feature shown in A-C; and (G–I) alluvial fan remnant and associated incised drainages at eastern CCW Site 2. The left panel of each row (A, D, G) shows the fault trace (pale blue ENE-trending line), topographic profiles used in the LaDiCaoz restoration (red and dark blue, ENE-trending lines), and the traces of the prominent offset features (red and dark blue dots, yellow lines) used in the restorations. Purple squares indicate projection of offset features to the fault. The middle panel of each row (B, E, H) shows our visually preferred 26 m restorations of each prominent feature. Right panels (C, F, I) show LaDiCaoz misfit derived from cross-correlating incrementally back-slipped topographic

profiles (see Zielke et al., 2015). Full results of these LaDiCaoz restoration are shown in Data Repository figures S2–S4.

Figure 6. Single grain K-feldspar post-IR IRSL data for youngest samples from unit 2 (the youngest alluvial fan unit we encountered at the CCW site) in each of our four sample pits, illustrating the method used in determining depositional ages (see Rhodes [2015] for further discussion). Each graph shows the equivalent dose estimates determined for that sample (labels to left of plots) for single grains, with results arranged in rank order sensitivity with data from the most sensitive grains to the left of each plot. For each of the four samples shown, 400 grains were measured, providing between 41 (J0116, J0294) and 63 (J0303) individual D_e estimates. Colored data points show grains that were included in age estimate calculations, open symbols represent data rejected from analysis. For two samples, small numbers of outlying low D_e value grains were rejected from the analysis (J0294, 1 grain; J0303, 2 grains), interpreted as post-depositional intrusive grains transported by bioturbation processes such as burrowing. For the remaining data, the statistical procedure described by Rhodes (2015) was used to select a combined equivalent dose estimate consistent with the minimum D_e values, using an over-dispersion value of 15% (red dashed lines). Note the high degree of consistency in this minimum value, in particular for samples J0294, J0298 and J0303. For sample J0116, which was inadvertently sampled across a sedimentary unit boundary between post-alluvial Unit 1 (likely representative of incipient infilling of depositional alluvial fan swales, possibly with an aeolian component) and unit 2, the shallowest alluvial fan unit we encountered, that was not clear when the pit was first excavated, we note a grouping of higher equivalent dose values, and have applied a finite mixture model to isolate a second D_e value shown in blue. We consider this value represents the depositional age for the shallowest alluvial unit in sample Pit 11A (i.e., alluvial fan Unit 2); our slip rate reconstructions are consistent with this, but do not require it to be so.

Figure 7. Log of North wall of trench excavated parallel to the Garlock fault to illustrate the relationship between the dated fan stratigraphy and the offset, incised channels used to determine the slip rate. Note sub-horizontal, laterally continuous alluvial fan strata of units 2-4 (post-alluvial unit 1 was not encountered at this location) that were erosionally truncated by incision of the offset drainage to the east ("active wash" in figure). This relationship demonstrates that incision of the now-offset drainages occurred after fan abandonment; indeed, we interpret the initial incision as the event that marks termination of active alluvial/fluvial deposition on the fans. Post-IR IRSL luminescence sample locations in pit 12A are shown by yellow circles at left edge of trench log; area of trench to left of "fold line" shows the west wall of sample pit 12A, which formed the western end of the trench (see figure 4a for location). Sub-rounded gray shapes denote large individual clasts. Depth and width are based on an arbitrary datum.

Figure 8. (A) Inferred incremental slip history of the central Garlock fault (solid red line) based on Christmas Canyon West ca. 1.9 ka slip rate (this study), paleo-earthquake ages from Dawson et al. (2003), mapping of small geomorphic offsets by McGill and Sieh (1991), and latest Pleistocene-early Holocene slip rates of McGill et al. (2009) and Ganev et al. (2012); thin, black vertical lines denote error ranges on paleo-earthquake ages. Suggested offsets in the ca. 5 ka and 7 ka earthquakes are based on inferred average offsets in the four most-recent earthquakes observed at EPP, assuming that the ~26 m of slip we document at the CCW site in this study also characterizes the total displacement at the EPP trench site of Dawson et al. (2003) during the

same time frame. Dashed red lines show possible early Holocene slip rates that would be required to explain both the well-constrained mid- to late Holocene incremental slip record and the longer-term rates of McGill et al. (2009) and Ganev et al. (2012). Lower panel shows age ranges of paleo-earthquakes from Dawson et al. (2003) El Paso Peaks trench site.

Figure 9. Plot showing incremental pattern of cumulative displacement on the Garlock and San Andreas faults over the past ca. 1600 years. Green line shows displacements and ages of two most recent Garlock fault earthquakes inferred from paleoseismic data of Dawson et al. (2003) and measurements of small geomorphic offsets from McGill and Sieh (1991). Orange boxes show age uncertainties for the most recent event and the penultimate event on the Garlock fault from Dawson et al. (2003). Small black crosses show displacement data for individual San Andreas fault surface ruptures and dashed blue line shows inferred incremental San Andreas fault slip rate curve based on those data from the Wrightwood site (Weldon et al., 2004). The incremental rate curve is drawn slightly differently from original curve in Weldon et al. (2004) to emphasize: (a) very slow SAF slip rate during the ca. 500-year-long period between 850–1550 AD earthquakes; and (b) the large displacement in the ca. 1500-1550 AD earthquake.

Table 1. Results of single-grain post-IR IRSL dating from the Christmas Canyon West site.

Supplementary Information Figure Captions

Supplementary figure S1. Uninterpreted lidar hillshade image of Christmas Canyon West study site showing the locations of our two study sites.

Supplementary figure S2. LaDiCaoz restoration of western alluvial fan remnant at Site 1 (on which pits 11A and 12C were excavated; see figure 3 in main text) and associated incised drainages. (A) Note fault trace (pale blue line), fault-parallel topographic profiles (dark blue and red lines), and along-feature profiles (dark blue and red dots, yellow lines) used din the reconstructions. Purple squares show projections of the offset features to the fault trace. Image is rendered by digitally draping lidar-derived topography (green-red colors) on top of a lidar hillshade map of the site. One meter contour intervals. Yellow dots bound the western lateral extent of the northern alluvial fan remnant. (B) Base image is similar to (A), but has been back-slipped by 23.5 m – the minimum sedimentologically plausible amount offset based on visual analysis. (C) Similar to (B), but back-slipped by 25.5 m, the optimal fit (i.e., minimum "misfit") based on LaDiCaoz cross-correlation of fault-parallel topographic profiles shown in (A). (D) Visually preferred restoration of 26.0 m, in close agreement with the optimal value determined by LaDiCaoz analysis. (E) Maximum sedimentologically plausible restoration of 29.5 m, based on visual analysis. (F) Topographic profiles from lidar swaths shown by red and dark blue fault-parallel lines in (A). Profiles are back-slipped according to the optimal topogrpahic fit determined by LaDiCaoz (25.5 m). (G) Topographic misfit as a function of horizontal displacement determined by cross-correlation of incrementally back-slipped topographic profiles (Zielke et al., 2015), showing minimum misfit at optimal 25.5 m for LaDiCaoz restoration.

Supplementary figure S3. LaDiCaoz restoration of prominent incised eastern edge of CCW Site 1 alluvial fan remnant associated incised drainage (location in figure 3 in main text). (A) Note fault trace (pale blue line), fault-parallel topographic profiles (dark blue and red lines), and along-feature profiles (dark blue and red dots, yellow lines) used in the reconstructions. Purple squares show projections of the offset features to the fault trace. Image is rendered by digitally draping lidar-derived topography (green-red colors) on top of a lidar hillshade map of the site. One meter contour intervals. Yellow dots bracket the eastern lateral extent of the northern alluvial fan remnant. (B) Base image is similar to (A), but has been back-slipped by 23.5 m – the minimum sedimentologically plausible amount offset based on visual analysis. (C) Similar to (B), but back-slipped by 26.0 m, the optimal fit (i.e., minimum “misfit”) based on LaDiCaoz cross-correlation of fault-parallel topographic profiles shown in (A). (D) Visually preferred restoration of 26.0 m is identical to the optimal value determined by LaDiCaoz analysis. (E) Maximum sedimentologically plausible restoration of 29.5 m, based on visual analysis. (F) Topographic profiles from lidar swaths shown by red and dark blue fault-parallel lines in (A). Profiles are back-slipped according to the optimal topographic fit determined by LaDiCaoz (25.5 m). (G) Topographic misfit as a function of horizontal displacement determined by cross-correlation of incrementally back-slipped topographic profiles (Zielke et al., 2015), showing minimum misfit at optimal 26.0 m for LaDiCaoz restoration.

Supplementary figure S4. LaDiCaoz restoration of alluvial fan remnant at Site 2 (on which pits 12A and 12B were excavated; see figure 3 in main text) and associated incised drainages. (A) Note fault trace (pale blue line), fault-parallel topographic profiles (dark blue and red lines), and along-feature profiles (dark blue and red dots, yellow lines) used din the reconstructions. Purple squares show projections of the offset features to the fault trace. Image is rendered by digitally draping lidar-derived topography (green-red colors) on top of a lidar hillshade map of the site. One meter contour intervals. Yellow dots bracket the eastern lateral extent of the northern alluvial fan remnant. (B) Base image is similar to (A), but has been back-slipped by 23.5 m – the minimum sedimentologically plausible amount offset based on visual analysis. (C) Similar to (B), but back-slipped by 25.7 m, the optimal fit (i.e., minimum “misfit”) based on LaDiCaoz cross-correlation of fault-parallel topographic profiles shown in (A). (D) Visually preferred restoration of 26.0 m is identical to the optimal value determined by LaDiCaoz analysis. (E) Maximum sedimentologically plausible restoration of 29.5 m, based on visual analysis. (F) Topographic profiles from lidar swaths shown by red and dark blue fault-parallel lines in (A). Profiles are back-slipped according to the optimal topographic fit determined by LaDiCaoz (25.5 m). (G) Topographic misfit as a function of horizontal displacement determined by cross-correlation of incrementally back-slipped topographic profiles (Zielke et al., 2015), showing minimum misfit at optimal 25.7 m for LaDiCaoz restoration.

Supplementary figure S5. Annotated photo log of sample Pit 11A (Site 1, south of fault) showing sample locations relative to stratigraphy exposed in the pit. Units 2 and 3 are medium brown alluvial/fluvial sands that are overlain in this pit by much paler-colored, friable post-alluvial fan unit 1. Note that sample J0116 was inadvertently collected across the stratigraphic boundary between units 1 and 2, which was not readily apparent until after the pit walls had dried somewhat, when the very different drying characteristics of units 1 and 2 became apparent. As is typical in all four pits from both alluvial fans studied at the CCW site, Unit 1 yielded very young ages (30±20 yb2013 and 790±70 yb2013 in this pit), whereas alluvial fan Unit 2 yielded a late Holocene age (2010±230 yb2013), and underlying alluvial fan Unit 3 yielded much older ages (3760±230 yb2013 and 3810±270 yb2013 in this pit).

Supplementary figure S6. Annotated photo log of sample Pit 12A (Site 2, south of fault) showing sample locations relative to stratigraphy exposed in the pit. Units 2, 3 a, 3b, and 3c are different alluvial/fluvial beds distinguished by textural and color differences. Some bedding planes are locally defined by gravel beds and lenses. This pit formed the western end of the short trench we excavated to better illustrate the relationship between the sub-horizontally bedded alluvial fan stratigraphy and the pos-fan abandonment incised drainges. As is typical in all four pits from both alluvial fans studied at the CCW site, uppermost alluvial fan Unit 2 yielded a late Holocene age (2620±190 yb2013 in this pit), and underlying alluvial fan Unit 3 yielded much older ages (4550±370 yb2013, 4740±290 yb2013, and 4470±360 yb2013 in this pit); post-alluvial fan Unit 1 was not encountered in this pit.

Supplementary figure S7. Annotated photo log of sample Pit 12B (Site 2, north of fault) showing sample locations relative to stratigraphy exposed in the pit. Sandy units 2, 3 a, 3b, and 3c are different alluvial/fluvial beds distinguished by textural and color differences. Some bedding planes are locally defined by gravel beds and lenses. Note that whereas sample J0298 (1860±150 yb2013) comes from gently southeast-dipping beds, underlying sample J099 (1910±150 yb2013), which yielded an almost identical IRSL age, was collected from a flat-lying alluvial bed. As is typical in all four pits from both alluvial fans studied at the CCW site, older alluvial fan Unit 3 yielded much older ages (4470±360 yb2013 and 7240±290 yb2013 in this pit); post-alluvial fan Unit 1 was not sampled in this pit.

Supplementary figure S8. Annotated photo log of sample Pit 12C (Site 1, north of fault) showing sample locations relative to stratigraphy exposed in the pit. Units 2 and 3 are different alluvial/fluvial beds distinguished by textural and color differences. These alluvial fan strata are overlain in this pit by much paler-colored, friable post-alluvial fan unit. Note that some bedding planes are locally defined by gravel beds and lenses. As is typical in all four pits from both alluvial fans studied at the CCW site, Unit 1 yielded a very young age (520±60 yb2013) in this pit, whereas Unit 2 yielded a late Holocene age (2280±140 yb2013 in this pit), and underlying Unit 3 yielded much older ages (4980±340 yb2013 and 5360±330 yb2013 in this pit).

IRSL Data Respository Text: Sample Preparation and Dating Methods

Samples were opened and prepared in the laboratory at UCLA under low-intensity red and amber lighting. Potassium feldspar grains of 175-200μm were separated from the central, unexposed, portion of each sample; following wet sieving to isolate the correct grain size range, samples were treated in dilute HCl to remove carbonate, dried, and the potassium feldspar component floated off using a lithium metatungstate (LMT) solution with a density of 2.58 $g.cm^3$. After rinsing, samples were treated in 10% hydrofluoric acid for 10 minutes to etch the outer surfaces of each feldspar grain, dried, and sieved at 175μm to remove small fragments.

Between 200 and 600 K-feldspar grains of each sample were measured using a post-IR IRSL SAR (single aliquot regenerative-dose) protocol modified for single grains from Buylaert et al. (2009), documented in Rhodes (2015). Measurements were made in a Risø TL-DA-20CD automated luminescence reader, fitted with an XY single grain attachment incorporating a 150 mW 830 nm IR laser passed through a single RG-780 filter to reduce resonance emission at 415 nm, used at 90% power for 2.5s. All measurements were made using a BG3 and BG39 filter combination, allowing transmission around 340 - 470 nm to an EMI 9235QB photomultiplier tube. For the natural measurement, and following each regenerative-dose and test dose application, a preheat of 250ºC for 60s was administered. IRSL was measured (for 2.5s for each grain) at 50ºC, and then subsequently at 225ºC (for the post-IR determination). Following a test dose of 9Gy, an identical preheat, IRSL at 50ºC and post-IR IRSL at 225ºC were administered. Each SAR cycle was completed with a hot bleach treatment using an array of Vishay TSFF 5210 870nm IR diodes at 90% power for 40s at 290ºC. The SAR sequence incorporated measurement of the natural IRSL, between four and six regenerative dose points, a zero dose point to assess thermal transfer, and a repeat of the first regenerative dose point, to assess recycling behavior.

Growth curves were constructed for the post-IR IRSL signal measured at 225ºC using an integral of the background-subtracted sensitivity-corrected IRSL from the first 0.5s, fitted with an exponential plus linear function. For most samples, around 5 to 10% of measured K-feldspar grains provided a useful post-IR IRSL signal, typically providing between 20 and 60 single grain results for each sample; other grains were either insensitive, associated with large uncertainties, or in the case of a few grains, the post-IR IRSL signal was in saturation. The upper samples, used to control slip rate, were measured using larger numbers of grains to improve statistical significance of the combined equivalent dose values. Samples typically displayed a uniform minimum equivalent dose value, with other grains displaying higher dose values, interpreted as grains incompletely zeroed before or during transport owing to rapid deposition from turbid water under high energy fluvial conditions. Most samples also displayed a small number of grains with significantly lower dose values, interpreted as intrusive grains introduced by bioturbation; these grains were excluded from the age analysis. Isolation of a population of grains for age estimation used a "discrete minimum" procedure in which higher values were excluded until the remaining grains were consistent with an overdispersion (OD) value of 15%, based on experience from quartz single grain OSL dating (e.g. Rhodes et al., 2010). Fading correction was based on detailed determination of single grain post-IR IRSL fading rates for key samples, and involve an increase in apparent age of 11%. Gamma dose rates were based on in-situ NaI spectrometer measurements; external beta dose rates were calculated from ICP-MS (U, Th) and ICP-OES (K) measurements of sediment from the end of each sample tube, internal beta dose rate was based on 12.5% internal K content, cosmic dose rates were based on measured overburden depth, and moisture correction used contemporary water content values.

References

Buylaert, J.P., Murray, A.S., Thomsen, K.J., Jain, M., 2009, Testing the potential of an elevated temperature IRSL signal from K-feldspar: Radiation Measurements, v. 44, p. 560-565.

Rhodes, E.J., 2015, Dating sediments using potassium feldspar single-grain IRSL: Initial methodological considerations: Quaternary International, v. 362, p. 14-22.

Rhodes, E.J., Fanning, P.C., Holdaway, S.J., 2010, Developments in optically stimulated luminescence age control for geoarchaeological sediments and hearths in western New South Wales, Australia: Quaternary Geochronology, v. 5, p. 348-352.

Figure 1

Click here to download Figure: Dolan et al. Garlock figure 1 resubmitted final.pdf

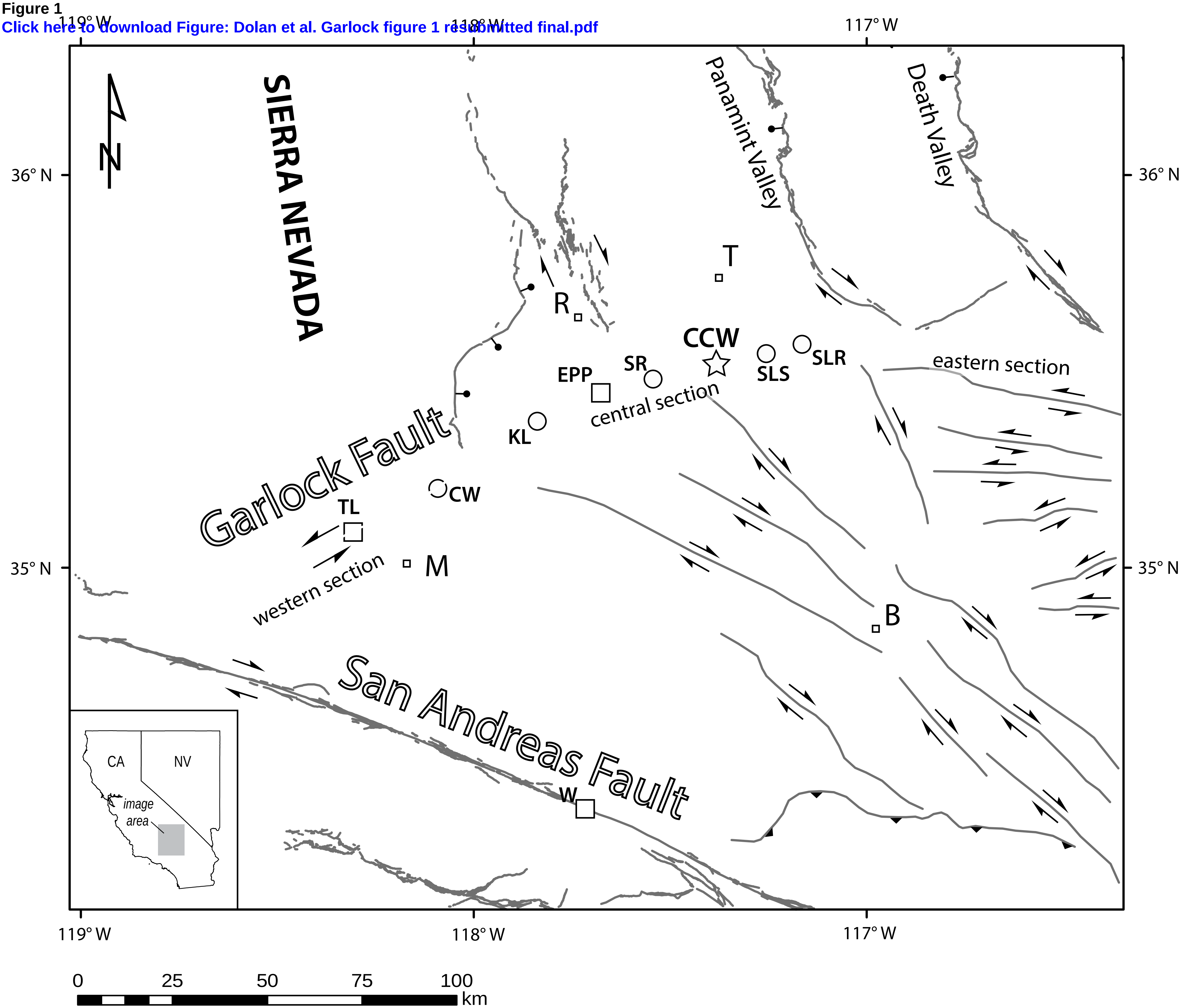

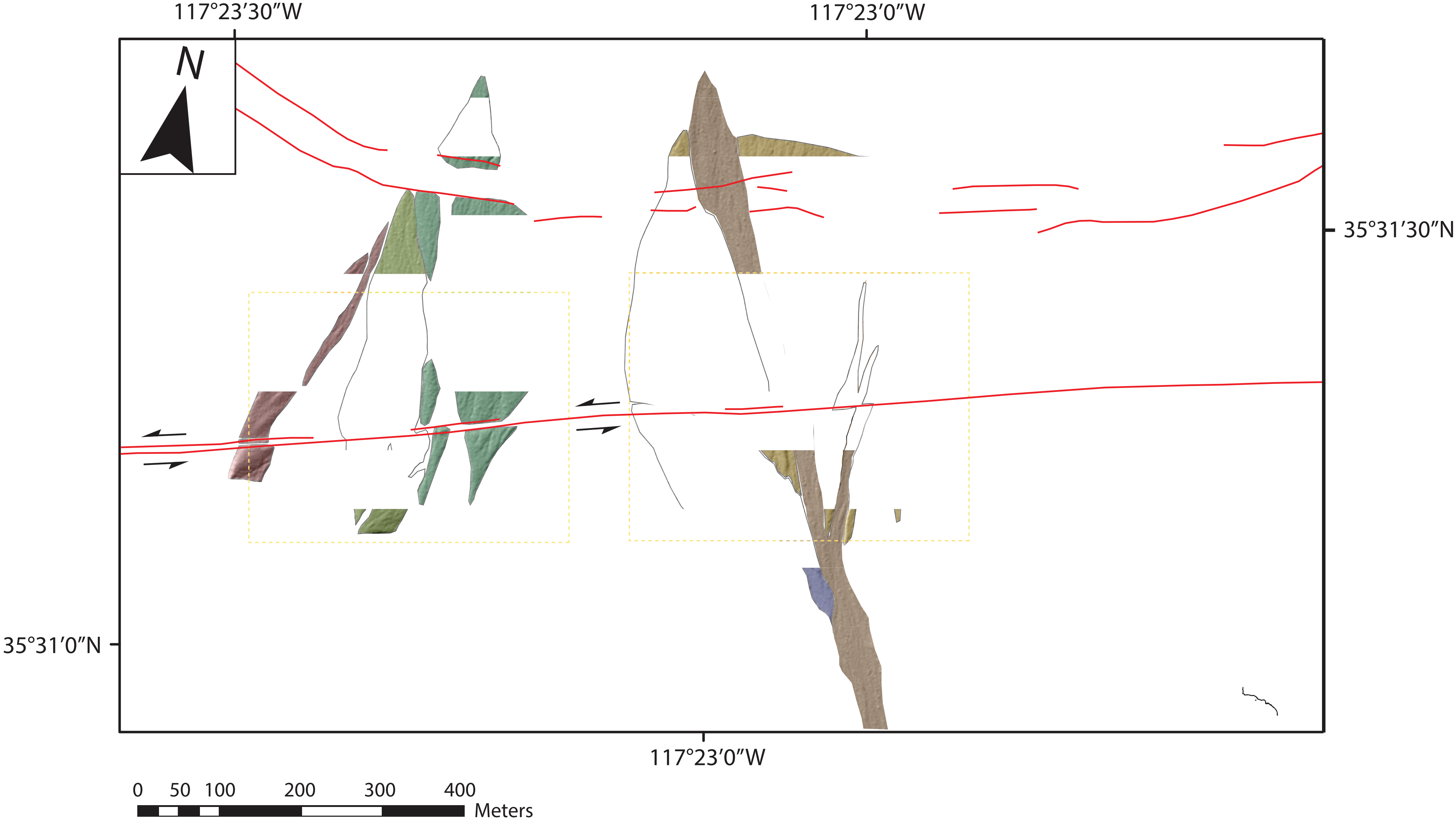
117°23′30″W
117°23′0″W
N
35°31′30″N
35°31′0″N
117°23′0″W
0
50
100
200
300
400
Meters

Figure 3
Click here to download Figure: Dolan et al. Garlock figure 3 resubmitted final.pdf

Figure 3

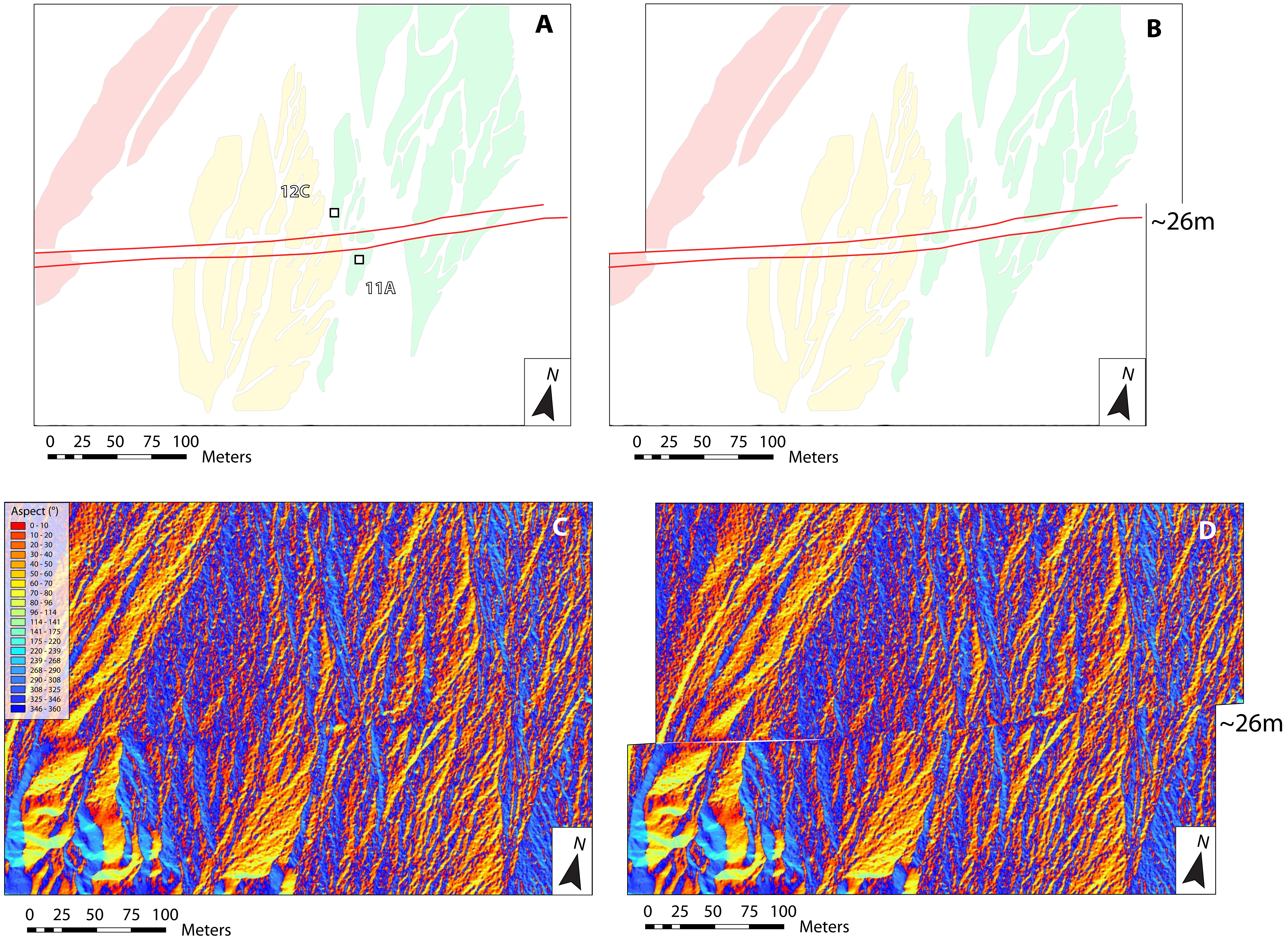

Figure 4
Click here to download Figure: Dolan et al. Garlock figure 4 resubmitted final.pdf

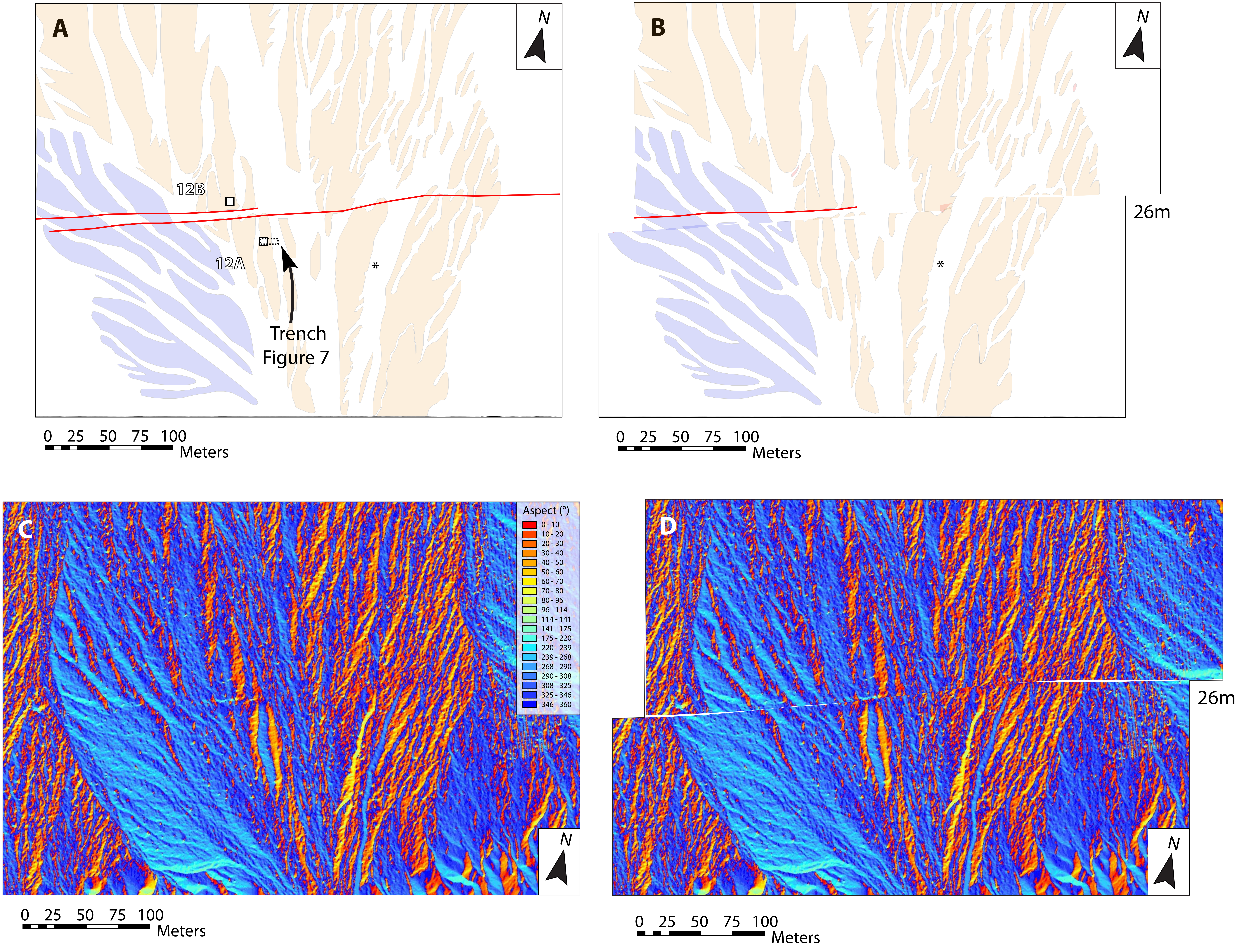

Figure 5
Click here to download Figure: Dolan et al. Garlock figure 5 final resubmitted.pdf
Figure 5

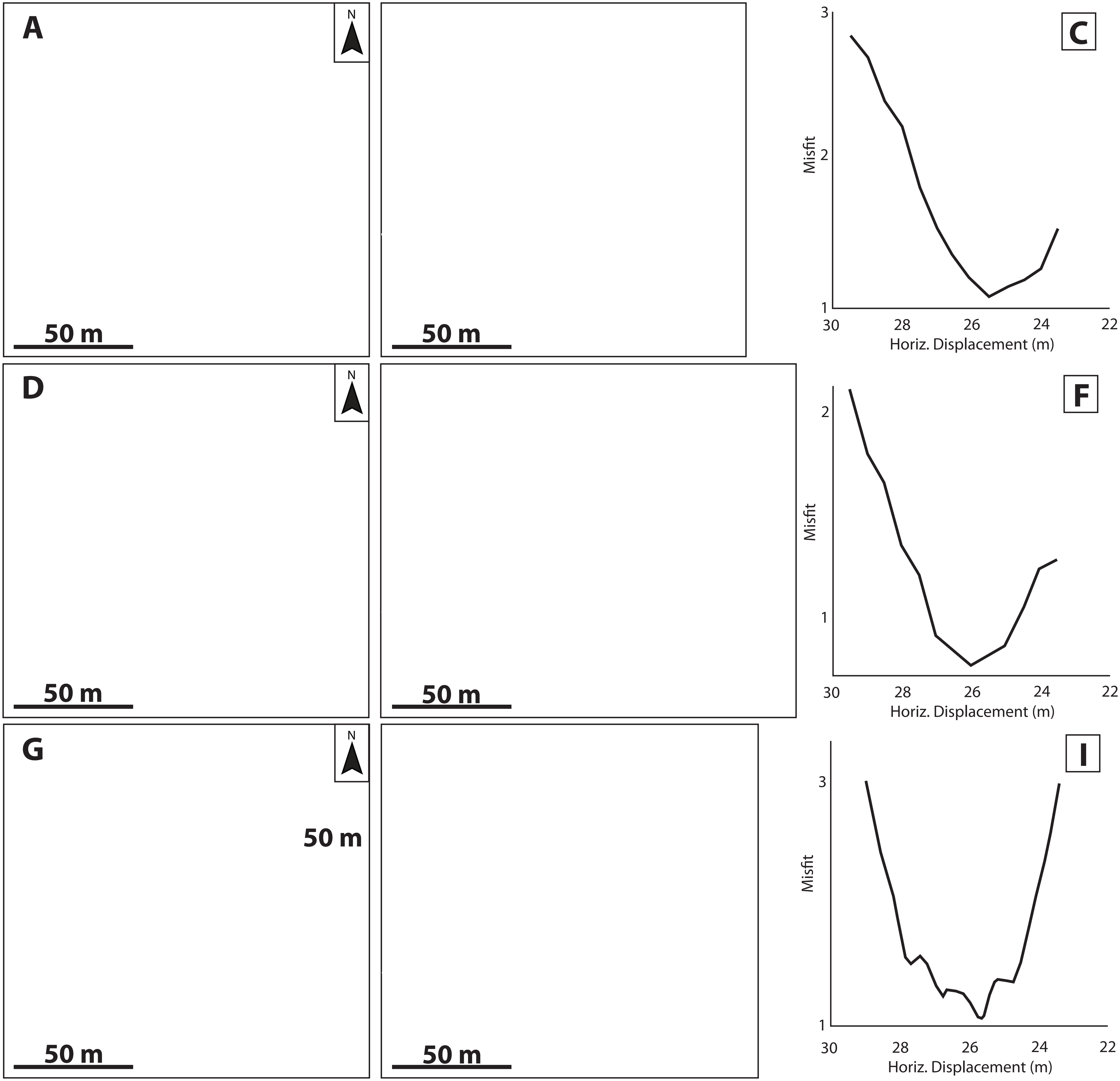

Figure 6

Click here to download Figure: Dolan et al. Garlock figure 6 final resubmitted.pdf

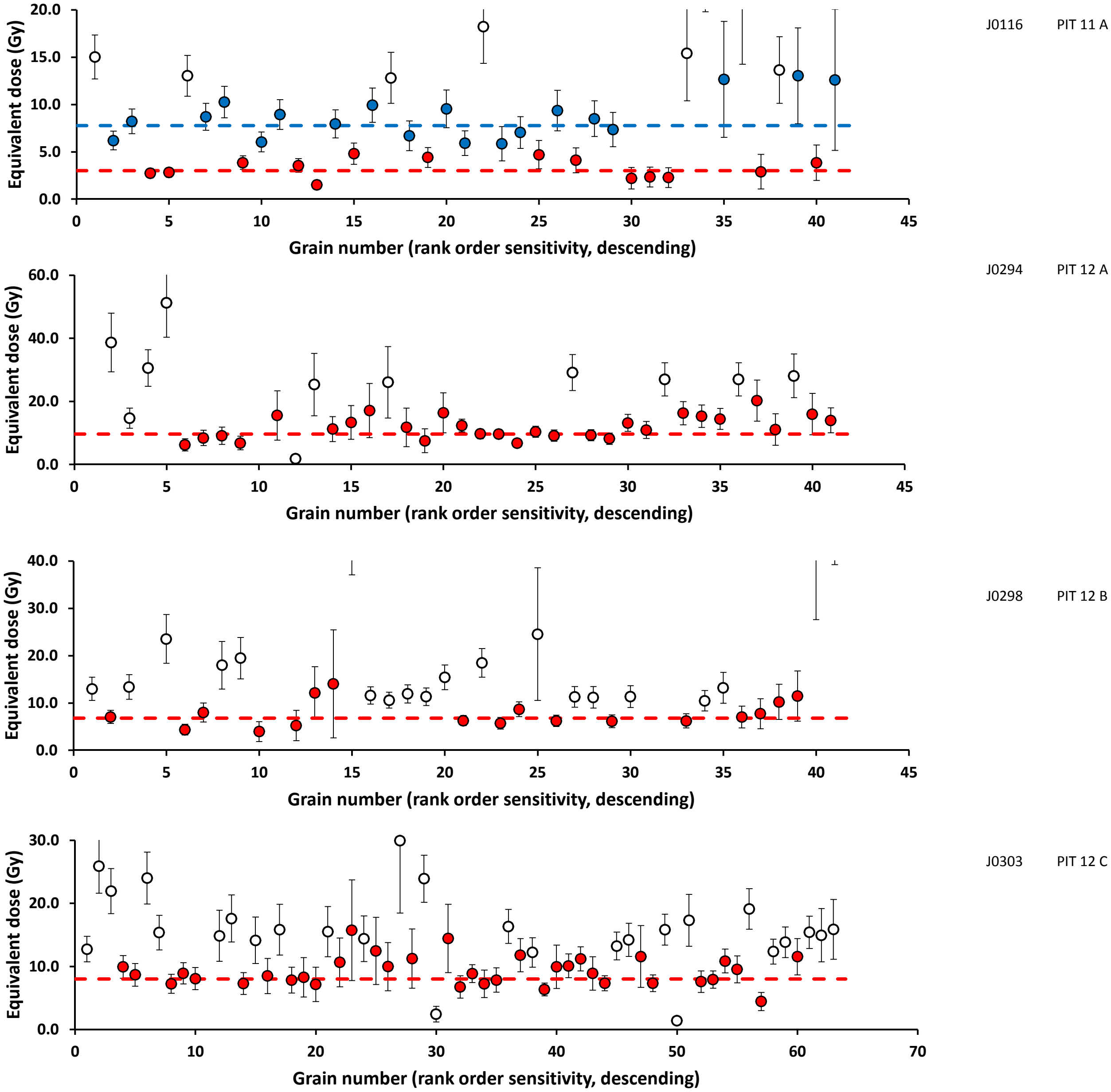

Figure 7
Click here to download Figure: Dolan et al. Garlock figure 7 final resubmitted.pdf

Figure 8

Click here to download Figure: Dolan et al. Garlock figure 8 final resubmitted.pdf

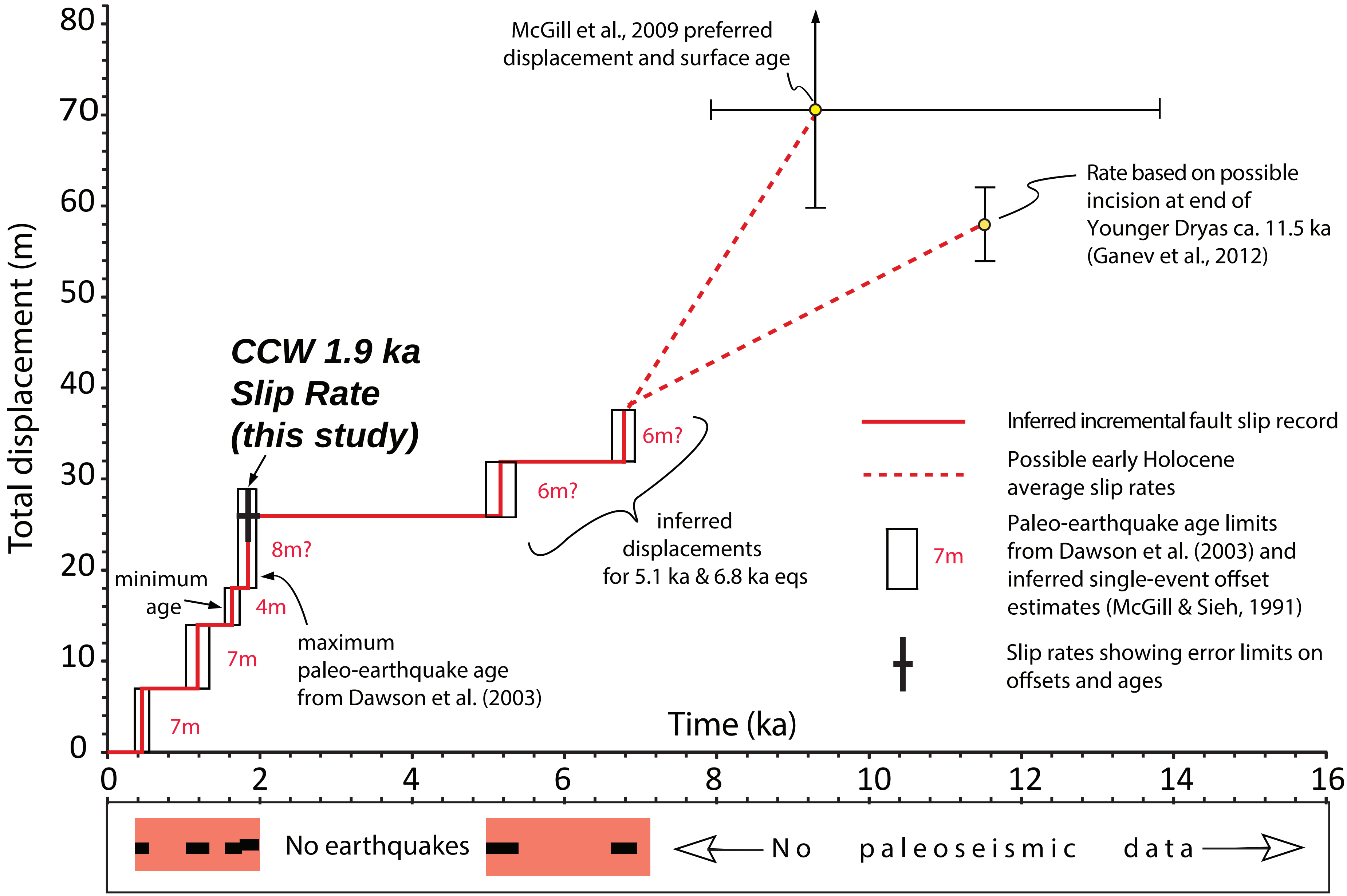

Figure 9

Click here to download Figure: Dolan et al. Garlock figure 9 final resubmitted.pdf

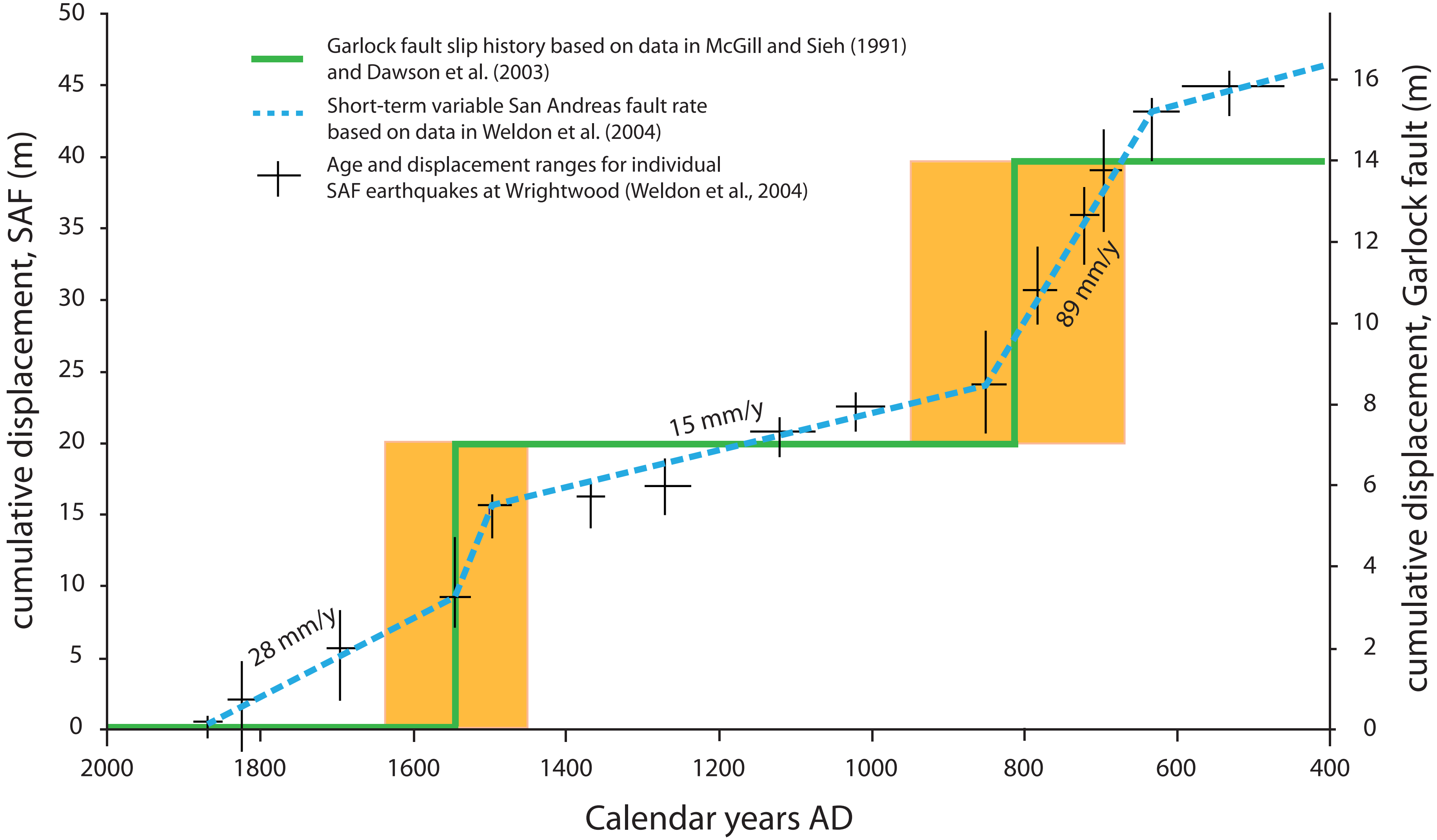

Figure S1

Click here to download Figure: Dolan et al. Garlock figure S1 final resubmitted.pdf

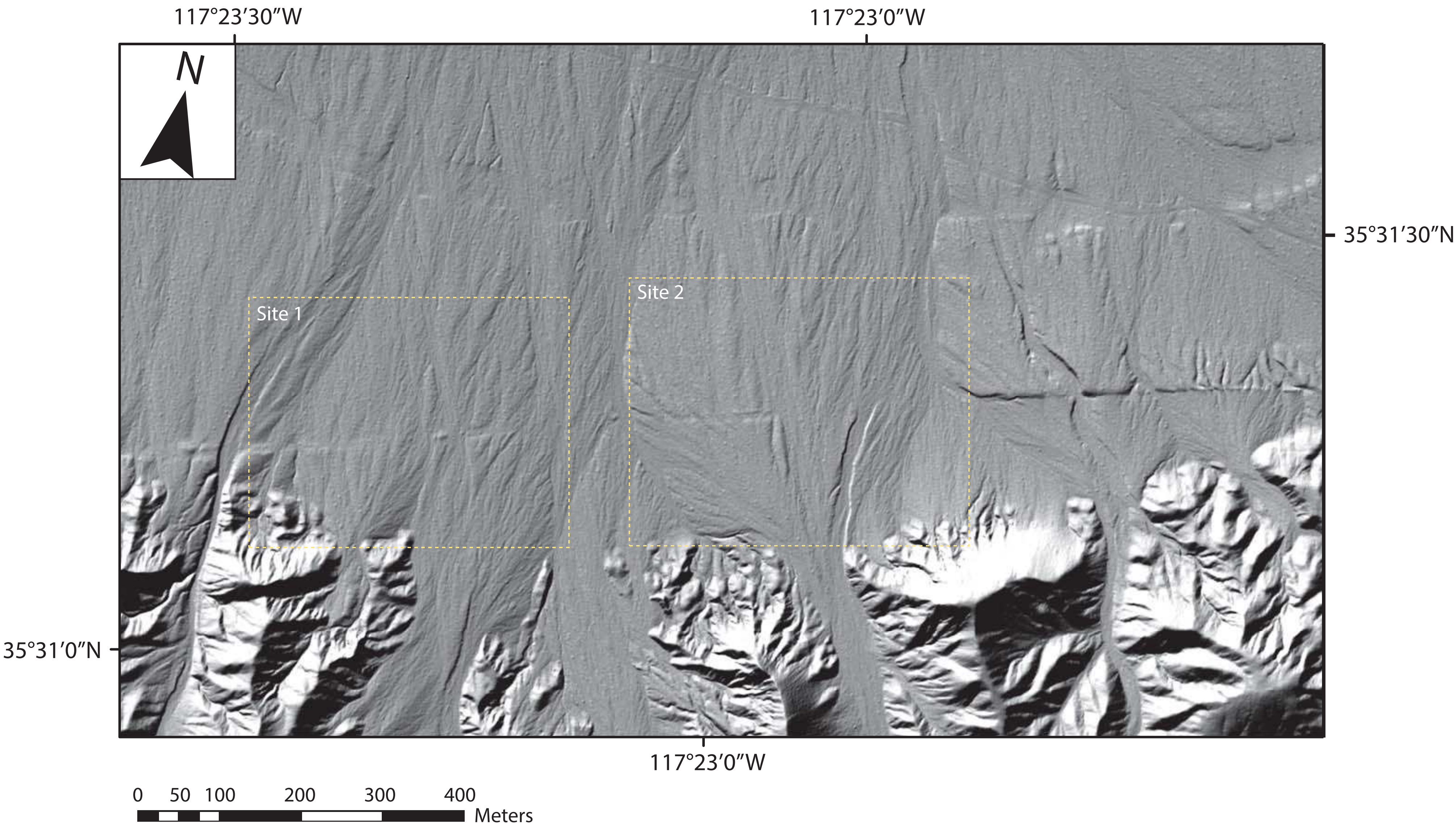

Figure S2

S2. LaDiCaoz restoration of alluvial fan remnant at Site 1

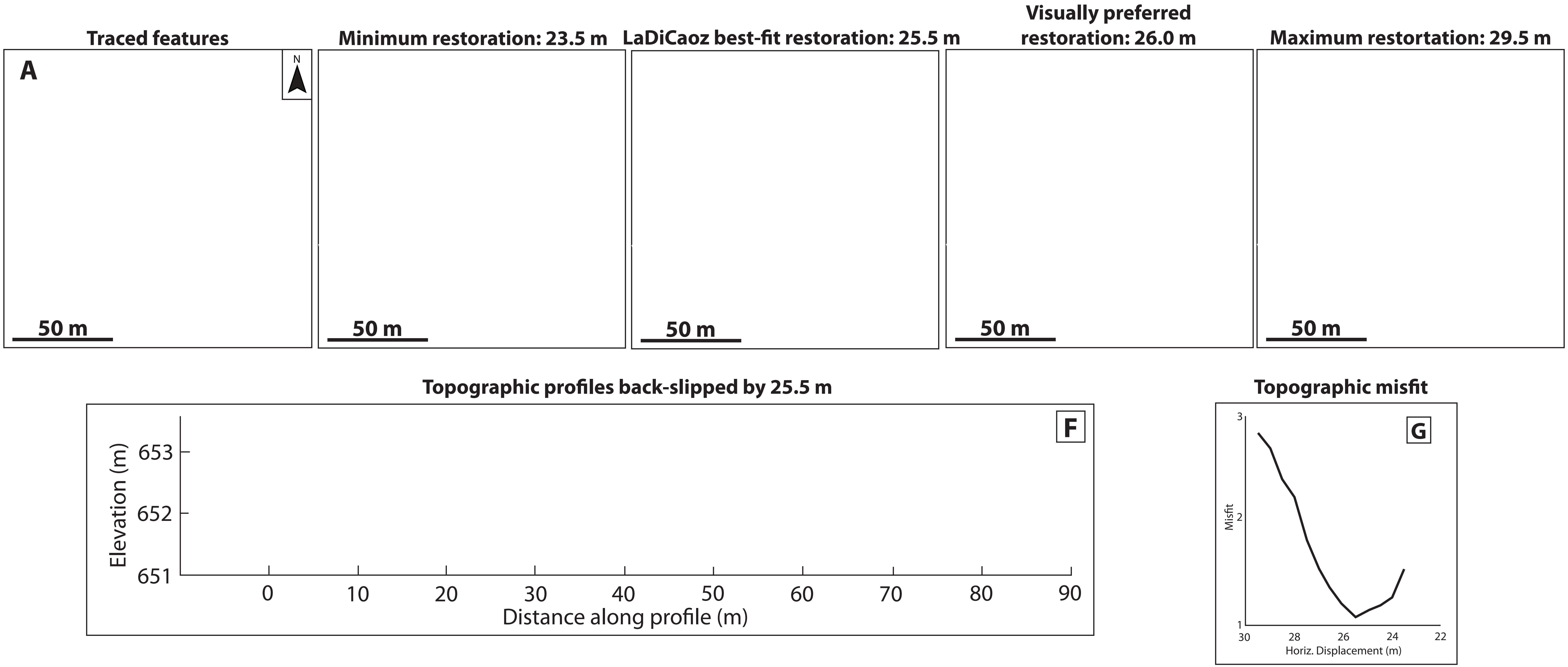

LaDiCaoz restoration of alluvial fan remnant at Site 1 (where pits 11A and 12C were excavated; see Fig. 3 in text) and several other minor drainages and intervening alluvial bars. (A) Tracings of fault trace (pale blue line), fault-parallel topographic profiles (dark blue and red lines), and along-feature profiles (dark blue and red dots, yellow lines). Purple squares are where the features project into the fault trace. Image is rendered by digitally draping lidar-derived topography (green-red colors) on top of a lidar hillshade map of the site. Contours represent 1 m intervals. Yellow dots bound the lateral extent of the northern alluvial fan remnant. (B) Base image is similar to (A), but has been back-slipped by 23.5 m -- the minimum sedimentologically plausible amount of offset based on visual analysis. (C) Similar to (B), but back-slipped by 25.5 m, the optimal fit (i.e., minimum "misfit") based on cross-correlation of fault-parallel topographic profiles shown in (A). (D) Visually preferred restoration of 26.0 m, in close agreement with the optimal value determined by LaDiCaoz analysis. (E) Maximum sedimentologically plausible restoration of 29.5 m, based on visual analysis. (F) Topographic profiles from lidar swaths shown by red and dark blue fault-parallel lines in (A). Profiles are back-slipped according to the optimal topogrpahic fit determined by LaDiCaoz (25.5 m). (G) Topographic misfit as a function of horizontal displacement determined by cross-correlation of incrementally back-slipped topogrpahic profiles (Zielke et al., 2015).

S3. LaDiCaoz restoration of eastern edge of alluvial fan and drainage, Site 1

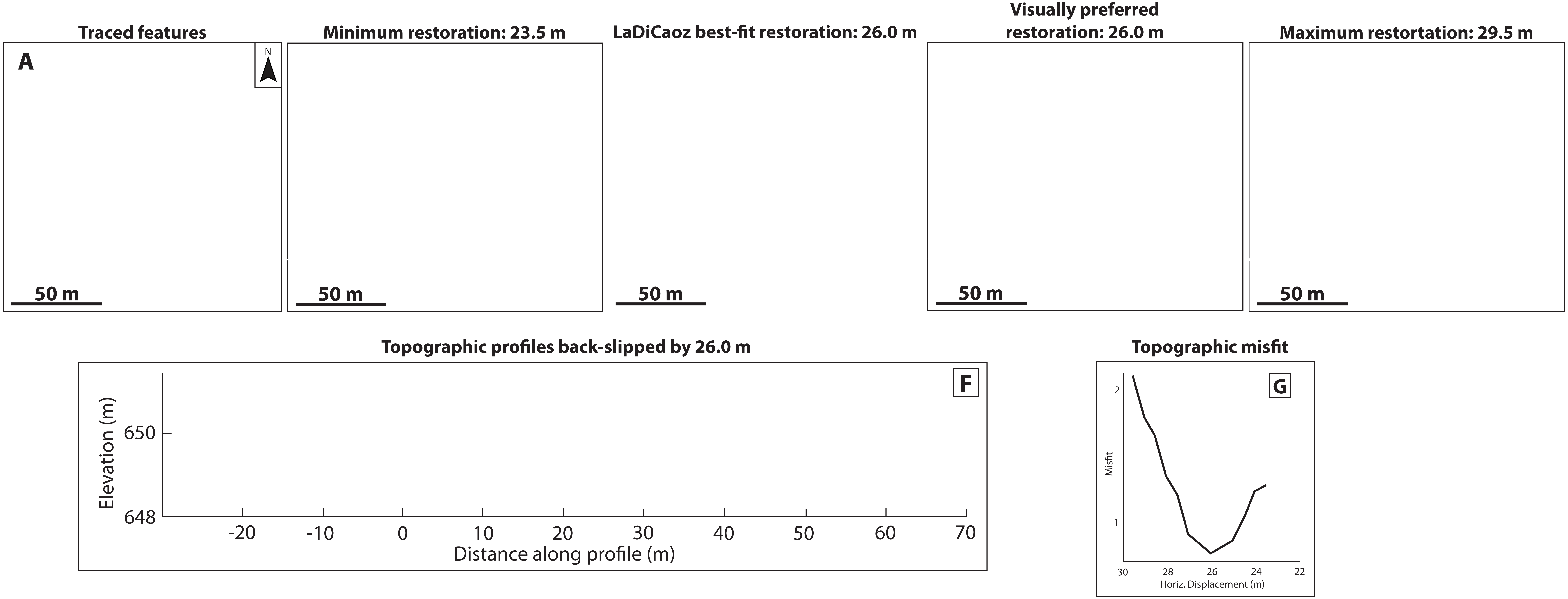

LaDiCaoz restoration of eastern edge of alluvial fan and associated NE-flowing drainage at Site 1 (see Fig. 3 in text). (A) Tracings of fault trace (pale blue line), fault-parallel topographic profiles (dark blue and red lines), and along-feature profiles (dark blue and red dots, yellow lines). Purple squares are where the features project into the fault trace. Image is rendered by digitally draping lidar-derived topography (green-red colors) on top of a lidar hillshade map of the site. Contours represent 1 m intervals. Yellow dots bound the lateral extent of the northern alluvial fan remnant. (B) Base image is similar to (A), but has been back-slipped by 23.5 m -- the minimum sedimentologically plausible amount of offset based on visual analysis. (C) Similar to (B), but back-slipped by 26.0 m, the optimal fit (i.e., minimum "misfit") based on cross-correlation of fault-parallel topographic profiles shown in (A). (D) Visually preferred restoration of 26.0 m agrees precisely with the optimal value determined by LaDiCaoz analysis. (E) Maximum sedimentologically plausible restoration of 29.5 m, based on visual analysis. (F) Topographic profiles from lidar swaths shown by red and dark blue fault-parallel lines in (A). Profiles are back-slipped according to the optimal topogrpahic fit determined by LaDiCaoz (26.0 m). (G) Topographic misfit as a function of horizontal displacement determined by cross-correlation of incrementally back-slipped topogrpahic profiles (Zielke et al., 2015).

S4. LaDiCaoz restoration of alluvial fan remnant at Site 2

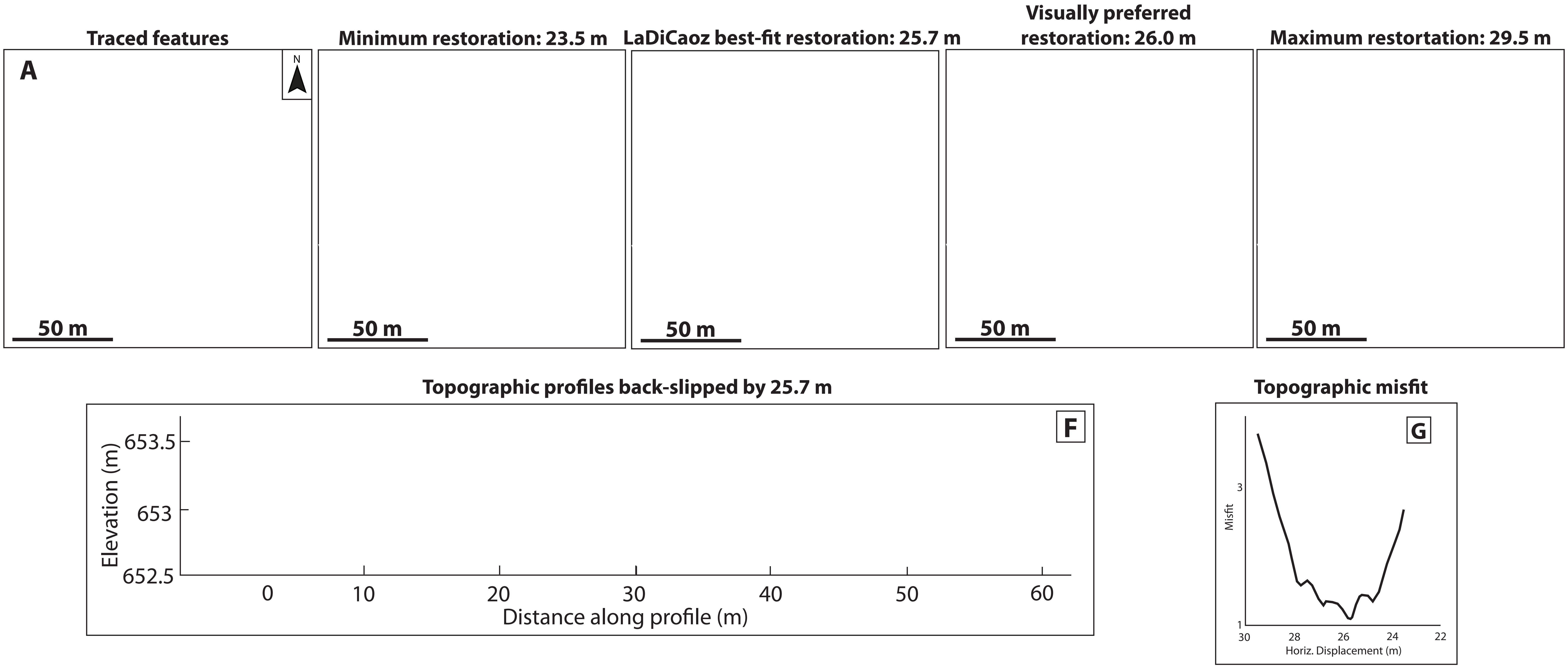

LaDiCaoz restoration of alluvial fan remnant at Site 2 (where pits 12A and 12B were excavated; see Fig. 4 in text) and associated drainages. (A) Tracings of fault trace (pale blue line), fault-parallel topographic profiles (dark blue and red lines), and along-feature profiles (dark blue and red dots, yellow lines). Purple squares are where the features project into the fault trace. Image is rendered by digitally draping lidar-derived topography (green-red colors) on top of a lidar hillshade map of the site. Contours represent 1 m intervals. Yellow dots bound the lateral extent of the northern alluvial fan remnant. (B) Base image is similar to (A), but has been back-slipped by 23.5 m -- the minimum sedimentologically plausible amount of offset based on visual analysis. (C) Similar to (B), but back-slipped by 25.7 m, the optimal fit (i.e., minimum "misfit") based on cross-correlation of fault-parallel topographic profiles shown in (A). (D) Visually preferred restoration of 26.0 m, in close agreement with the optimal value determined by LaDiCaoz analysis. (E) Maximum sedimentologically plausible restoration of 29.5 m, based on visual analysis. (F) Topographic profiles from lidar swaths shown by red and dark blue fault-parallel lines in (A). Profiles are back-slipped according to the optimal topogrpahic fit determined by LaDiCaoz (25.7 m). (G) Topographic misfit as a function of horizontal displacement determined by cross-correlation of incrementally back-slipped topogrpahic profiles (Zielke et al., 2015).

S5. Christmas Canyon West, Pit 11A
View of IRSL samples and gamma spectrometer measurements, S wall of pit

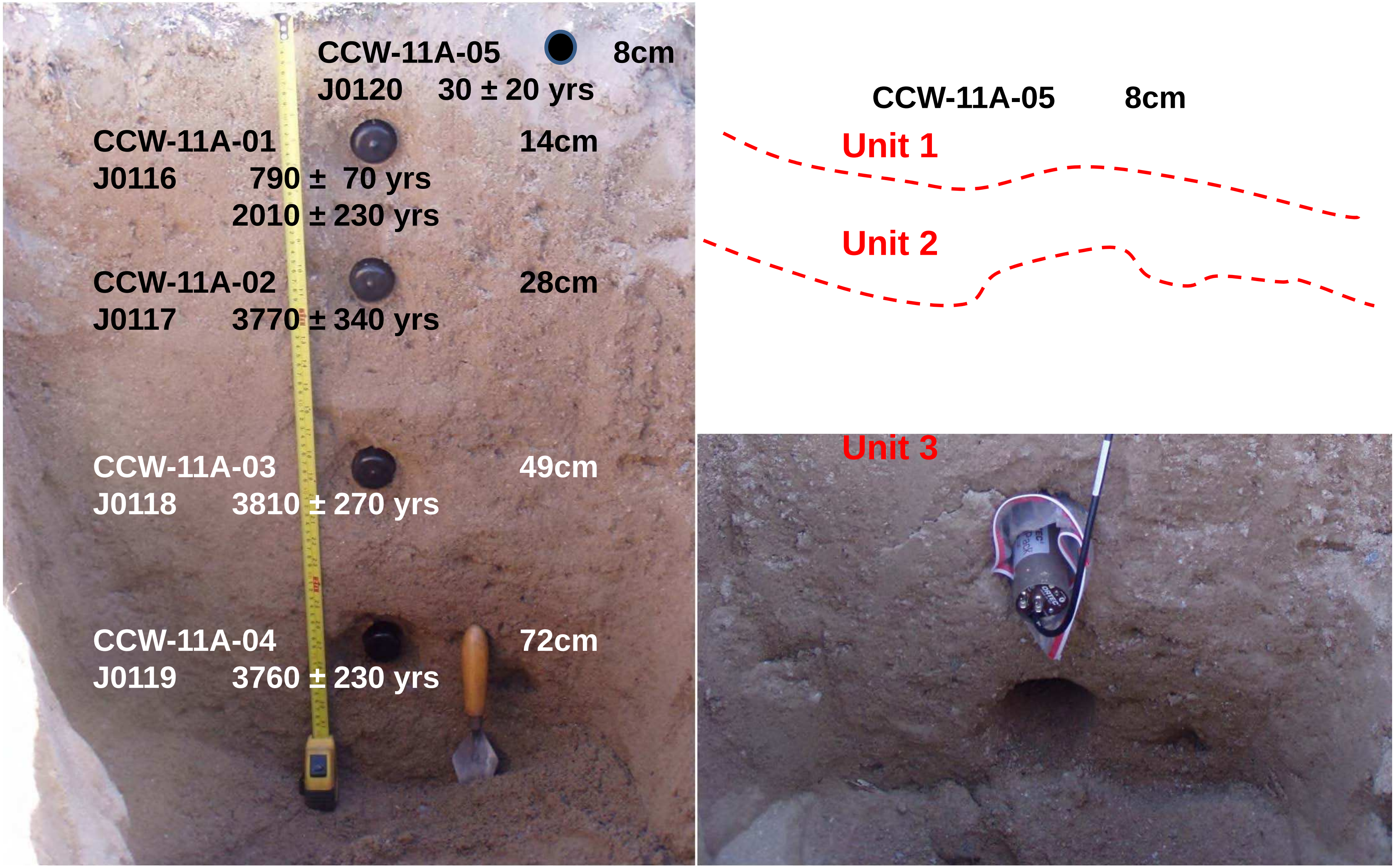

S6. Christmas Canyon West, Pit 12A
View of IRSL sample locations and gamma spectrometer holes, W wall of pit

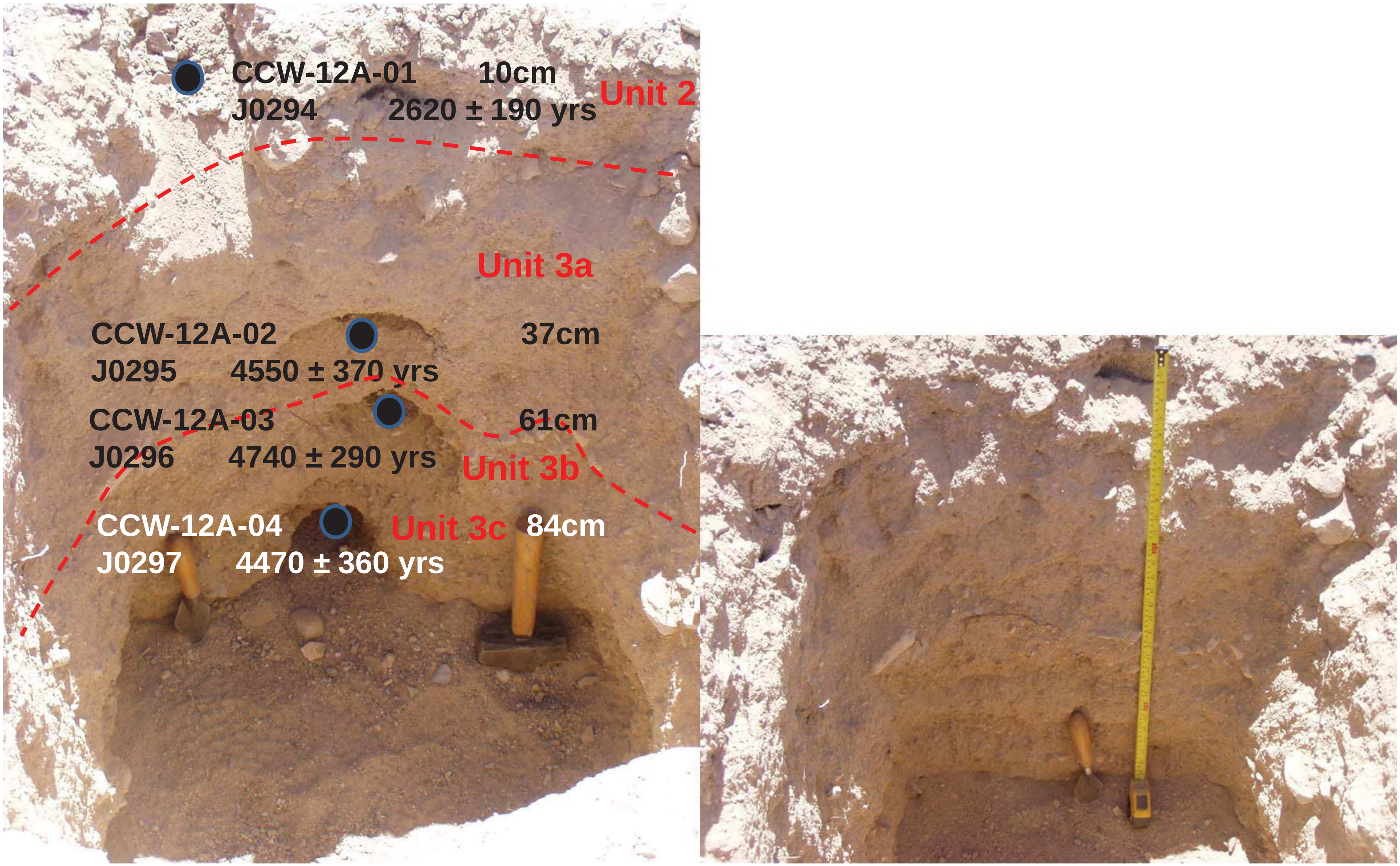

S7. Christmas Canyon West, Pit 12B
View of IRSL sample locations and gamma spectrometer, W wall of pit

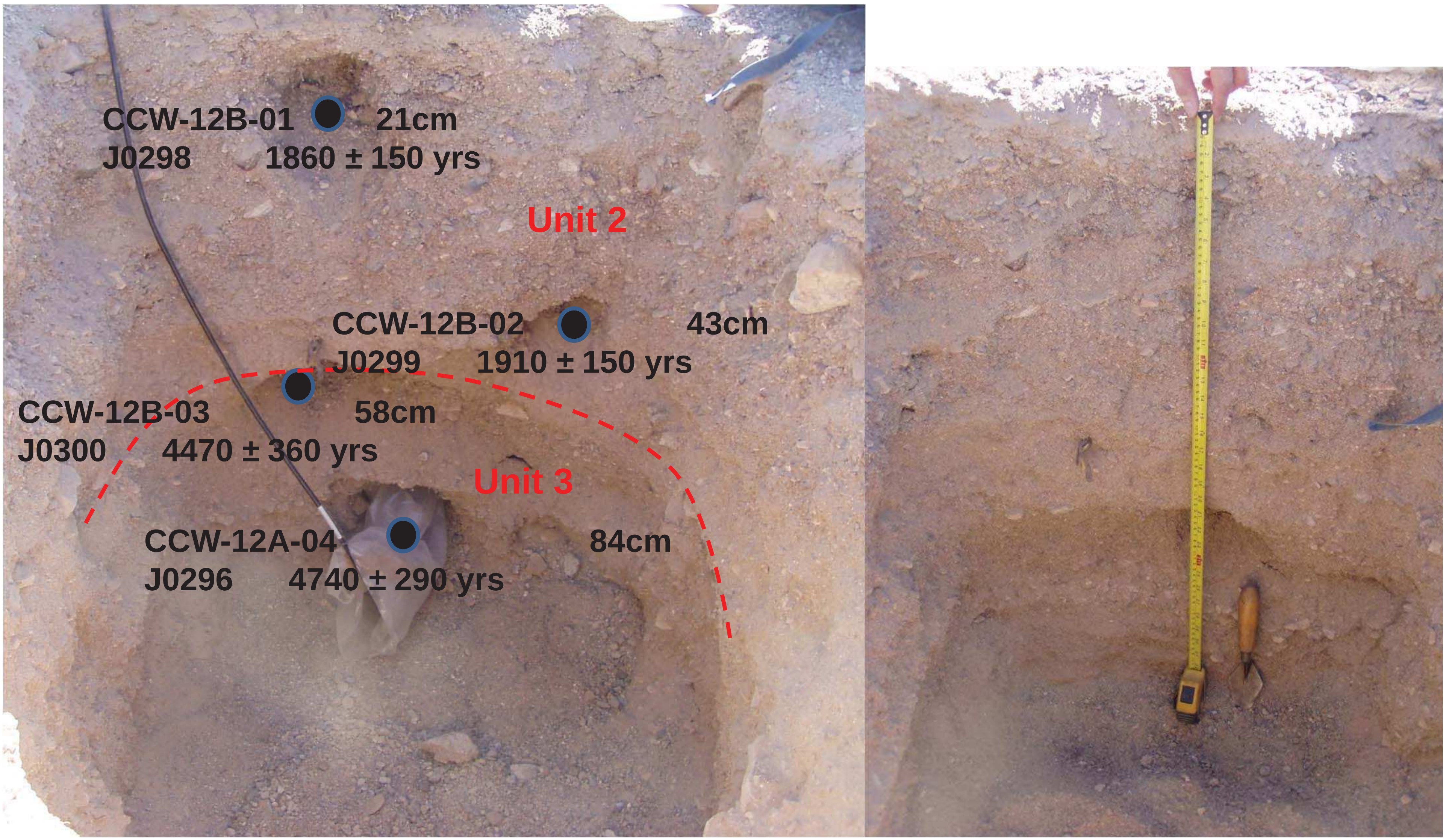

S8. Christmas Canyon West, Pit 12C
View of IRSL sample locations and gamma spectrometer, W wall of pit

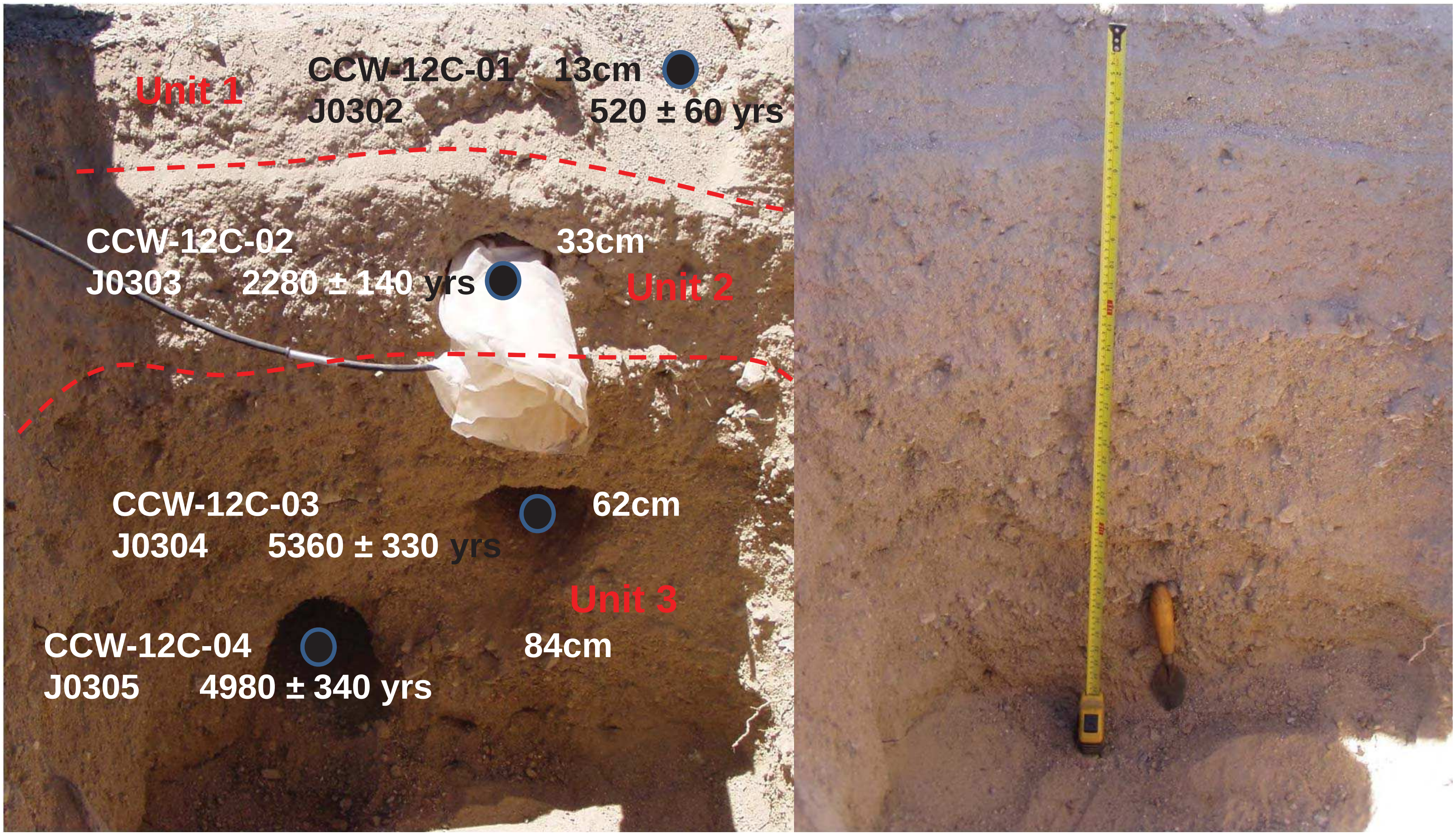

Site code	Pit code	Field code	Lab code	Strat unit	Depth (m)	Age (years)		1 sigma uncertainty
1	11A	CCW11A05	J0120	Unit 1	0.08	30	±	20
1	11A	CCW11A01	J0116	Unit 2	0.14	790	±	70
1	11A	CCW11A02	J0116	Unit 2	0.14	2010	±	230
1	11A	CCW11A02	J0117	Unit 3	0.28	3770	±	340
1	11A	CCW11A03	J0118	Unit 3	0.49	3810	±	270
1	11A	CCW11A04	J0119	Unit 3	0.72	3760	±	230
1	12C	CCW12C01	J0302	Unit 1	0.13	520	±	60
1	12C	CCW12C02	J0303	Unit 2	0.29	2280	±	140
1	12C	CCW12C03	J0304	Unit 3	0.62	5360	±	330
1	12C	CCW12C04	J0305	Unit 3	0.84	4980	±	340
2	12A	CCW12A01	J0294	Unit 1	0.10	2620	±	190
2	12A	CCW12A02	J0295	Unit 2	0.37	4550	±	370
2	12A	CCW12A03	J0296	Unit 3a	0.61	4740	±	290
2	12A	CCW12A04	J0297	Unit 3b	0.84	4470	±	360
2	12B	CCW12B01	J0298	Unit 1	0.21	1860	±	150
2	12B	CCW12B02	J0299	Unit 1	0.43	1910	±	150
2	12B	CCW12B03	J0300	Unit 2	0.58	4700	±	290
2	12B	CCW12B04	J0301	Unit 2	0.84	5620	±	360